

**THE ESTABLISHMENT OF THE LUMINOSITY FUNCTION FOR BROWN
DWARF CANDIDATES IN GAIA EARLY DATA RELEASE 3**

by

Dylan M. Hilligoss

A thesis submitted to the Faculty of the University of Delaware in partial fulfillment of the requirements for the degree of Master of Science in Physics

Summer 2022

© 2022 Hilligoss
All Rights Reserved

**THE ESTABLISHMENT OF THE LUMINOSITY FUNCTION FOR BROWN
DWARF CANDIDATES IN GAIA EARLY DATA RELEASE 3**

by

Dylan Hilligoss

Approved: _____
John Gizis, Ph.D.
Professor in charge of thesis on behalf of the Advisory Committee

Approved: _____
Edmund Nowak, Ph.D.
Chair of the Department of Physics and Astronomy

Approved: _____
John Pelesko, Ph.D.
Dean of the College of Arts & Sciences

Approved: _____
Louis F. Rossi, Ph.D.
Vice Provost for Graduate and Professional Education and
Dean of the Graduate College

ACKNOWLEDGMENTS

Perhaps the question I get asked most often as an astrophysicist is “are we alone in the universe?” While this question is still hotly debated across the globe, I can happily say that I have never felt alone during the process of completing this thesis. I am indebted to many people for making the work presented here possible, and to some for helping me maintain some semblance of sanity throughout it all.

First and foremost are my parents, Tina and Mike, who have never wavered in their support of my endeavors. Without their excellent parenting, I would not be the person I am today. All those years of them challenging me to push myself to the next level have allowed me to pursue opportunities that I never thought possible. I cannot thank them enough for their love, for keeping me motivated throughout difficult times, and for urging me to be the best person I can be. Now, the next time my father says “make us proud,” I can know with confidence that I am doing just that.

My advisor, John Gizis, has been the cornerstone of my research education. He took me on as a mere undergraduate in physics many years ago where I instantly felt a connection. During our many research meetings throughout my undergraduate and graduate careers, he has taught me the true meaning of dedication and hard work. From our time working with the Large Synoptic Survey Telescope to our current mission investigating brown dwarfs, he has taught me how to embrace difficult tasks while still having some fun along the way. Without his infectious passion for brown dwarfs, I would not have come to realize the beauty of this seemingly obscure branch of astrophysics.

I would like to extend my deepest thanks to a former professor and mentor of mine, Stan Owocki. Perhaps the most important thing he has taught me is to take a step back and look at the bigger picture – what is the basic physics, what do we learn, why is this interesting, how can this be applied to other astrophysical processes – questions that have helped me stay focused in the rapidly blossoming field of brown dwarf astronomy. He has always challenged me to take complex physical phenomena and break them down into their most fundamental principles which has proved to be invaluable while collaborating and communicating my results to others both within and outside of the scientific community.

I would like to pay my sincere regards to the other members of my thesis committee – James MacDonald and Veronique Petit – who have graciously accepted my invitation to read and critique this work. I am honored to work with these esteemed astronomers as they help push me along the path to success.

Finally, this project would not have been possible without the help from many within the University of Delaware’s Department of Physics and Astronomy. From the department chair, Ed Nowak, and the front office staff, to professors, peers, and colleagues, I am extremely thankful for the continued support they have provided me – academically, professionally, and socially – during my many years at the University of Delaware.

TABLE OF CONTENTS

LIST OF FIGURES	vii
ABSTRACT	x
PREFACE: What is a Brown Dwarf?	xi
Chapter	
1 BACKGROUND MATERIAL	1
1.1 Introduction	1
1.2 Brown Dwarf Astronomy	1
1.2.1 Perspectives Throughout History	2
1.2.2 Internal Physics	5
1.2.3 Fusion Processes in Brown Dwarfs	9
1.2.4 Life and Evolution	14
1.2.5 Atmospheres	17
1.3 Summary	20
2 MODES OF ANALYSIS	22
2.1 Introduction	22
2.2 <i>GAIA</i>	22
2.3 Color-Magnitude Diagram	28
2.4 Tangential Velocities	31
2.5 The Luminosity Function	34
2.6 Summary	37
3 RESULTS	39
3.1 Introduction	39
3.2 <i>GAIA</i> Luminosity Functions	40
3.3 Theoretical Brown Dwarf Models	43
3.3.1 Sonora Substellar Models	43
3.3.2 CLES Stellar Models	45
3.3.3 Combining the Models	47
3.3.4 Bolometric Magnitude to <i>GAIA</i> G-Band Magnitude	51
3.4 Interpretations of Theoretical Models and <i>GAIA</i> Luminosity Function	53
3.5 Summary	57

CONCLUSIONS	59
REFERENCES	63

LIST OF FIGURES

Figure 1	Evolution of the core temperature as predicted by Burrows et al. (1997) and shown by Burgasser (2002). Each line represents objects of masses 1, 5, 10, 13 (planets, “dot-dashed lines”) 20, 30, 42, 52, 63, 68, 75 (brown dwarfs, “solid line”) 80, 90, 100 M_J (stars, “dashed lines”). Also denoted are the lower limits for deuterium (T_D), lithium (T_L), and hydrogen fusion (T_H). 5
Figure 2	Evolution of the ratio of nuclear to total luminosity over time as predicted by Burrows et al. (1997) and shown by Burgasser (2002). The lines are the same as those of Figure 1.1. Regions of deuterium, lithium, and hydrogen burning are also noted. 9
Figure 3	Illustration of evolutionary tracks for objects with different, indicated masses and how their effective temperatures relate to lithium depletion from Basri et al. (1998). The hatched region to the right of the plot shows where lithium is being depleted. The stippled region on the lower half of the indicates where the presence of lithium guarantees a substellar object regardless of age. 12
Figure 4	Evolution of effective temperature in low-mass dwarfs as predicted by Burrows et al. (1997, solid lines) & Chabrier et al. (2000a, dashed lines) and presented by Burgasser (2002). From left to right and bottom to top, the lines represent masses of 10, 20, 30, 40, 50, 60, 70, 75, 80, 90, and 100 M_{Jup} 13
Figure 5	Evolution of luminosity for red dwarfs and substellar objects with solar metallicity from Burrows et al. (2001). Stars are denoted by blue lines, brown dwarfs above 13 M_{Jup} are denoted with green lines, and brown dwarfs/giant planets are given by red lines. The masses of these objects range from 0.3 M_{Jup} to 211 M_{Jup} ($0.2M_{\odot}$). The brown dots show where 50% of available deuterium has been burned and the purple dots indicate where 50% of available lithium has been burned. .. 13
Figure 6	This figure taken from Burrows et al. (2001) shows the evolutionary tracks of substellar objects of different masses (lines and color schematic are the same as those of Figure 5). Also denoted is the radius of Jupiter. Note that the radii are not monotonic with mass and that they settle to values around that of R_{Jup} in later times, despite the wide range of masses represented. 15

Figure 7	Color-Magnitude Diagram of GCNS data using G-RP color index and absolute magnitude in the G band. This figure clearly shows the location of the main sequence (high density region going from top left to bottom right). Also depicted in this figure is the Red Giant Branch turnoff (outcropping located at the top of the main sequence). For reference, the sun would lie near the center of the main sequence. Potential brown dwarfs would lie in and around the tail extending from the bottom of the main sequence as indicated by the arrow. 28	28
Figure 8	Color-Magnitude Diagram of Figure 7 zoomed in on the bottom tail of the main sequence where potential brown dwarfs would reside. 29	29
Figure 9	Shows a histogram of tangential velocities for all stars in GCNS with $0.0 < M_G < 20.0$. Most stars in the sample have tangential velocities less than 50km/s. 32	32
Figure 10	Histogram of a subset of GCNS with $14.0 < MG < 20.0$ and $1.0 < G - RP < 3.0$ magnitude and color constraints. This subset encompasses brown dwarf candidates. It is easily seen that most stars in this sample have tangential velocities between 20-40km/s. 33	33
Figure 11	This figure shows the luminosity function of the GCNS sample computed for absolute <i>GAIA</i> magnitudes $0.0 < MG < +20.0$ counted in 0.25 magnitude bins on a linear scale. A noticeable peak occurs around $MG \approx +11.0$ 40	40
Figure 12	This figure shows the luminosity functions of the constrained GCNS sample for objects with $vt \leq 20\text{km/s}$ (blue curve) and $vt \geq 100\text{km/s}$ (red curve) with the aforementioned color and magnitude constraints (i.e. $1.00 < G - RP < 3.00$ and $+14.0 < MG < +20.0$) and separate into 0.25 magnitude bins. The functions have been normalized to each other in order to overplot them. In both cases, the luminosity function steadily decreases as magnitude increases. 42	42
Figure 13	This figure shows the mass-luminosity relationship for the combined metal-poor models from Marley et al. (2021) and Fernandes et al. (2019). The mass ratio ranges from 0.015-0.013. The data was linearly interpolated for 1000 masses to provide a smooth relationship. The increase in luminosity around the mass ratio of 0.07 indicates that the HBMM lies at this point. Also note that there is no discontinuity between the two models due to the slight metallicity difference. 46	46

Figure 14	This figure shows the mass-luminosity relationship for the combined solar metallicity models from Marley et al. (2021) and Fernandes et al. (2019). Again, the mass ratio ranges from 0.015-0.13 and was linearly interpolated for 1000 masses. An increase still occurs around $0.07M_{\odot}$ corresponding to the onset of nuclear fusion but is not as pronounced as in the metal-poor model.	47
Figure 15	This figure shows the linearly interpolated mass-temperature relationship for 1000 masses between $0.01M_{\odot}$ and $0.13M_{\odot}$. The data comes from the combined metal-poor models from Marley et al. (2021) and Fernandes et al. (2019). There is a dramatic increase in temperature around the HBMM. At low and high masses, though, the temperature only gradually increases.	49
Figure 16	This figure shows the linearly interpolated mass-temperature relationship for 1000 masses between $0.01M_{\odot}$ and $0.13M_{\odot}$. The data comes from the combined solar metallicity models produced by Marley et al. (2021) and Fernandes et al. (2019). There is a large temperature change around the HBMM, but at low and high masses, the temperature slowly increases.	49
Figure 17	This figure shows the relationship between absolute bolometric magnitude and <i>GAIA</i> 's absolute magnitude in the G-band as derived from EDR3 and Filippazzo et al. (2015). Applying a linear curve fit emphasizes the seemingly linear nature of this relationship.	52
Figure 18	This figure shows a comparison between the observational luminosity function obtained from <i>GAIA</i> 's GCNS sample (black curve) and the combined models from Marley et al. (2021) (orange histogram) and Fernandes et al. (2019) (blue histogram) for 10 Gyr aged metal-poor objects. The observational luminosity function matches well with the stellar regime and penetrates into the high mass end of the brown dwarf regime.	54
Figure 19	This diagram shows a comparison between the observational luminosity function obtained from <i>GAIA</i> 's GCNS sample (black curve) and the combined models from Marley et al. (2021) (orange histogram) and Fernandes et al. (2019) (blue histogram) for objects 10 Gyr aged objects with solar metallicity. The observational luminosity function matches with the stellar regime. The observational luminosity function also enters into the upper end of the brown dwarf regime in this case.	55

ABSTRACT

Brown dwarfs are classified as objects with masses between that of stars and planets. First theorized in the 1960s, they remained an elusive target for detection until the mid 1990s since they have no sustainable energy source therefore causing them to cool and become less luminous over time. With the advent of more sophisticated telescopes, such as *GAIA*, astronomers have been able to probe to higher magnitudes/lower luminosities leading to the discovery of numerous confirmed brown dwarfs over the past two decades. Here, I examine the luminosity function from a set of brown dwarf candidates derived from *GAIA*'s Catalogue of Nearby Stars (GCNS) by applying a classical technique that makes use of the space density over defined intervals of absolute magnitudes. I then present a comparison between *GAIA*'s observational luminosity function and predictions from current brown dwarf models for both metal poor and metal rich objects. I find that *GAIA* is a great tool for investigating the properties of objects surrounding the critical hydrogen burning minimum mass but does not penetrate deep into the brown dwarf regime due to absolute magnitude limitations of the spacecraft. I also highlight the importance of metallicity when classifying objects near the stellar/substellar boundary and find that small variations can significantly alter this boundary.

PREFACE: What is a Brown Dwarf?

One of the most gratifying aspects of pursuing a career in astronomy is the absolute fascination people have about my field of study. Some of my conversations evolve into profound discussions about topics such as early cosmic evolution, the multiverse theory, and the existence of aliens; while others revolve around the latest breakthroughs including the first images of a black hole, the endless discoveries of extra-solar planets, and the presence of water on Mars. However, on occasion, I'll stumble across an inquisitive person who wants to know what, specifically, it is that I do. These conversations lead inexorably to the question, "So what even is a brown dwarf?"

To the substellar astronomer, the answer to this question is straightforward. But for many others, the term "brown dwarf" refers to a distant and mysterious object that sits on the borders of understanding. Though not as flashy and popular as gravitational waves or asteroid mining, brown dwarfs can still provide an excellent basis for understanding much of the universe.

Such is the popular unawareness in a field that takes a back seat to other areas of astronomy. Though brown dwarfs were theorized as early as the 1960s by Shiv Kumar and Chushiro Hayashi as well as Takenori Nakano, it was not until just before the turn of the century that their existence was confirmed by observational evidence. Indeed, the first bona-fide brown dwarf, Teide 1, was discovered in 1995 by astrophysicists Rafael Rebolo López, María R. Zapatero-Osorio and Eduardo L. Martín from the Teide Observatory on the island of Tenerife in the Canaries (Rebolo et al. 1995). That same year, astronomers Rebecca Oppenheimer, Keith Matthews, Tadashi Nakajima, and Shrinivas Kulkarni from Caltech made another unimpeachable

brown dwarf discovery with their observations of Gliese 229B (Oppenheimer et al. 1995). I had very little exposure in the field of substellar astronomy before I began my study at the University of Delaware. These objects were still barely covered in any of my prior astronomy courses, so I completely understand the lack of publicity brown dwarfs have received until a relatively short time ago. For the longest time, they lived in obscurity behind the ubiquitous stars and planets that populate a large fraction of the scientific literature in astronomy. So why are they even worth studying if no one has ever seen them with his or her own eyes?

To understand the draw of brown dwarfs, what they are, and their significance to astronomy, it is useful to examine their history. As in many other fields, brown dwarf astronomy got off to a slow start. After the initial theories were proposed by Kumar, Hayashi, and Nakano, it wasn't until the mid 1980s that brown dwarf research really took off. This decade saw rapid developments in theoretical models, observing techniques, and terminology. The term "brown dwarf," coined by astronomer Jill Tarter some ten years earlier to describe the unknown spectral energy distributions of these enigmatic objects became accepted as the nomenclature around this time.

The allure of brown dwarfs only intensified as the theories matured. In an effort to be the first to observe these objects, members of the brown dwarf community undertook various extensive searches of nearby stars and stellar clusters using ground and space-based telescopes. Why the sudden explosion of interest? Well, theories proposed that brown dwarfs could provide the solution to the dark matter problem. Others studied them for the purpose of examining lower limits of stellar formation. Still others took it one step further by proposing that brown dwarfs could exist in multi-star systems; perhaps even explaining mass-extinction events on Earth by

suggesting that the Sun has a periodic substellar companion – dubbed “Nemesis.” But perhaps the most important reason for this eruption of brown dwarf research derives from the simple fact that they had not yet been observed. This was an entirely new frontier in astronomy that pushed the limits of our technology and could extend our knowledge of stellar and substellar properties.

The astronomer is motivated by two key things: to develop physically meaningful theories, and to back these theories up with observational evidence. The theories had been proposed, so the hunt began.

This hunt lasted for many years before it bore fruit.

Around the mid-1990s, substellar objects started to be discovered in young star clusters and as companions to nearby stars. With these observational findings came the discovery of Teide 1 as well as Gliese 229B. Gliese 229B, discovered by Tadashi Nakajima, Ben Oppenheimer, David Golimowski, and Shri Kulkarni also in 1995, was found orbiting a nearby low-mass star, Gliese 229A. After these two groundbreaking finds, it wasn't long until numerous other brown dwarfs started to be found. Some were found as solo, “free-floating” objects while others were found as companions or as in stellar clusters. With this, the observational age of brown dwarf astronomy had officially begun.

Now the question became, why were brown dwarfs so hard to spot? What makes them so dim? To answer this, we need to understand the nature of these objects. What powers them? What are their environments like? Just like normal stars, brown dwarfs are born in star forming regions through the process of gravitational contraction of giant molecular clouds. Over time, this falling mass collects on a dense stellar core forming an accretion disk, as discovered by Fernando Comeron and

August Muench along with others. This accretion disk is eventually cleared which enables them to settle into a normal evolutionary pattern. The key difference between a normal star and a brown dwarf arises from the fact that, for some reason, they do not accumulate enough mass to ignite hydrogen thermonuclear fusion. The central core temperature and pressure is simply not high enough for this process to be sustained. Without these nuclear fusion reactions, objects less massive than 0.075 solar masses will radiate away their potential energy causing them to cool and dim over time. This lack of hydrogen fusion is what defines brown dwarfs and separates them from main sequence stars.

Over the ensuing two and a half decades, much more has been learned regarding these substellar objects. With the help of ever-more sophisticated technology, we have studied the internal physics and light-element fusion that powers brown dwarfs as well as the life and evolution of these objects. Further brown dwarf searches have shown that they have atmospheres primarily consisting of H₂, H₂O, and CH₄; only possible for bodies with low enough temperatures. In fact, Gliese 229B was found to have an effective temperature of well over 500K less than the coolest observed stars making it more akin to a planet in the eyes of some. Gliese 229B was a unique case until our spectral classification system was expanded to include L and T dwarfs as more and more substellar objects were found. J. Davy Kirkpatrick defined T dwarfs as objects with the same spectral appearance as Gliese 229B; mainly, the existence of CH₄ absorption in the near infrared. Kirkpatrick theorized that many objects similar to Gliese 229B existed but just had not been discovered yet. But as more extensive searches in the infrared zone of the electromagnetic spectrum were conducted, more such substellar bodies were found.

Now with brown dwarf astronomy in full swing, I entered the picture. My goal was to approach this subject from a different angle in the hopes of gaining some new insight into brown dwarfs using the latest available data from sources such as the Global Astrometric Interferometer for Astrophysics (hereafter referred to as *GAIA*). Specifically, my aim was to examine the luminosity function (number of objects per volume per luminosity range) for a set of nearby stars and constrain this catalogue into a viable luminosity function for a subset of brown dwarf candidates.

My hope is that the following pages will further illuminate the evolution of brown dwarf and substellar astronomy and how the creation of such luminosity functions will contribute to our overall comprehension of these small, faint, and once mysterious objects.

Chapter 1

BACKGROUND MATERIAL

1.1 Introduction

In this chapter, we address and review some background material pertaining to the subject of substellar, brown dwarf astronomy. Throughout section 1.2, we discuss the basic physics of brown dwarfs by drawing upon previous work conducted by various esteemed theorists. Specifically, material regarding historical perspectives and key figures who have contributed to the development of the field over the last number of decades is covered. Next, we examine the basic internal physical properties of brown dwarfs followed by a discussion of fusion processes occurring in these substellar objects. Additionally, we cover the life and evolution of brown dwarfs and how they diverge from that of standard stars. Brown dwarf atmospheres are also addressed within this section to highlight some of the significant predicted and observed differences between them and main sequence stars. Finally, the material covered is recapitulated and interpreted in section 1.3.

1.2 Brown Dwarf Astronomy

Brown dwarf astronomy is still a relatively young. Over the past number of decades since brown dwarfs were first theorized then ultimately discovered, we have learned much about their extreme interiors. Burrows et al. (2001) shows that $\rho_c \sim 10 - 10^3 \frac{\text{g}}{\text{cm}^3}$, $T_c \propto 10^6 \text{K}$, and $P_c \sim 10^5 \text{Mbar}$. These extreme interior conditions test our understanding of degenerate plasmas and light element fusion processes, while the

molecular-rich atmospheres have led to new developments in line opacity formation and atmospheric dynamics. We have learned much about how these objects power and sustain themselves as well as how they evolve over cosmic time. But much remains to be understood.

1.2.1 Perspectives Throughout History

The objects that are now referred to as “brown dwarfs” have a history that covers a diverse range of subfields in physics. From quantum and classical mechanics, to high-pressure dynamics and atmospheric chemistry, brown dwarfs provide the link between the lowest-mass stars and the highest-mass planets.

The theoretical study of what would later become known as brown dwarfs got started by Kumar (1963) and Hayashi & Nakano (1963) who both independently predicted that below some minimum mass, roughly $0.08M_{\odot}$, electron degeneracy would halt the gravitational collapse of a protostar prior to the start of hydrogen nuclear fusion. Hayashi & Nakano (1963) proposed this minimum mass limit would hold true for both Population I and Population II stars. Objects less massive than this minimum mass never reach a central core temperature high enough to fuse hydrogen into helium. Thus, over time, they will cool down. These objects were coined as “brown dwarfs” by astronomer Jill Tarter (1975) and the nomenclature has stuck ever since.

The evolution of these brown dwarfs was further studied by Hoxie (1970) and Grossman, Hays, & Graboske (1974) by making detailed calculations of their interior physics. Grossman, Hays, & Graboske (1974) included in their calculations the effects of light-element fusion and electron screening while also first predicting that deuterium-burning occurs down to a lower mass limit of $0.012M_{\odot}$. A number of

astronomers including but not limited to Stevenson (1978), Vandenberg et al. (1983), D'Antona & Mazzitelli (1985), Lunine, Hubbard & Marley (1986), and Burrows, Hubbard & Lunine (1989) provided additional early work on brown dwarf evolution through their analysis of atmospheres, metallicity, dust opacity, convection, and mass fraction and luminosity dependences. Throughout the late 1970s and into the 1980s, the basic picture of brown dwarfs grew and expanded. By the end of the 1980s, they were thought of as high-pressure, fully convective, and predominately degenerate bodies that decrease in temperature through the steady loss of thermal and gravitational potential energy over time.

The 1990s saw more advances in theories of brown dwarf interior physics and atmospheres. Saumon, Chabrier, & Van Horn (1995) rigorously defined the equation of state for hydrogen and helium in the high-pressure, low-temperature environments present in brown dwarf interiors. They included the effects of phenomena like internal pressure and ionization rates which have a substantial impact on the evolution of these objects. Saumon et al. (1994) and Baraffe et al. (1995) made significant advances in evolutionary models by using non-grey atmospheres. Furthermore, Mould (1975, 1976) developed the first atmospheric models for M dwarfs, or hot brown dwarfs. Allard et al. (1996), and Marley et al. (1996) later developed cool brown dwarf atmospheric models mainly in response to the discovery of Gliese 229B in 1995. These early atmospheric models were able to excellently reproduce some of the gross characteristics that were observed in early brown dwarf discoveries such as the existence of CH₄ in Gliese 229B and spectral reddening by dust opacity. Though these models did fail to explain other key features such the red slope found in the optical band of cooler L and T dwarfs.

The first observational discoveries of brown dwarfs in 1995 drew the attention of numerous other astronomers. Allard (2001) conducted detailed studies and produced opacity models of atmospheres, spectra, and colors for brown dwarfs while Burrows, Marley, & Sharp (2000) did work understanding the infrared and optical spectra of methane-dominant dwarfs and brown dwarfs. But over the last two decades, the majority of brown dwarf research has been through the identification, cataloguing, and analysis of large data sets. With our ever-increasing technological capabilities, we have been able to refine our searches to identify more and more bona fide brown dwarfs. Ground and space-based observational surveys have been conducted using the Two Micron All Sky Survey (2MASS), the SLOAN Digital Sky Survey, various observatories such as the Keck Observatory in Hawaii and Teide Observatory in the Canaries off the eastern coast of Africa, and more recently, missions such as the Transiting Exoplanet Survey Satellite (*TESS*) and *GAIA*.

Now with the recent launch of the James Webb Space Telescope (*JWST*), which will conduct space-based imaging in infrared wavelengths, brown dwarf astronomers are waiting with bated breath for the newest era of discoveries to begin.

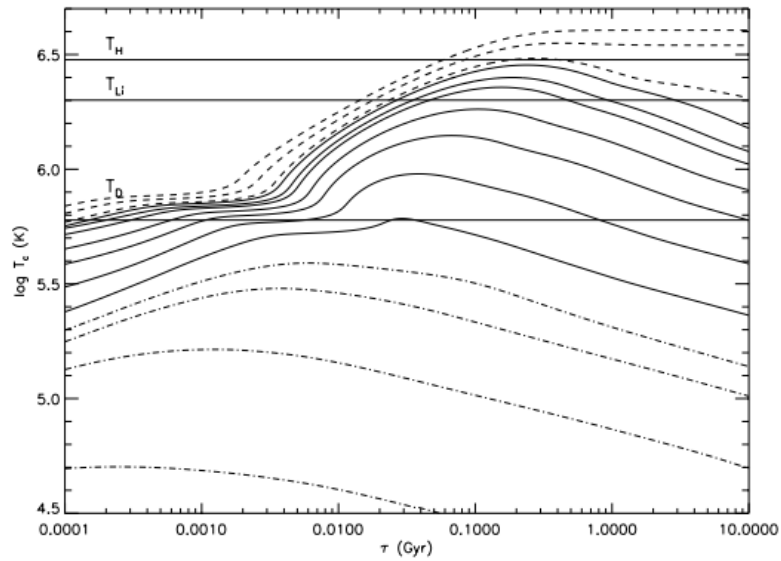


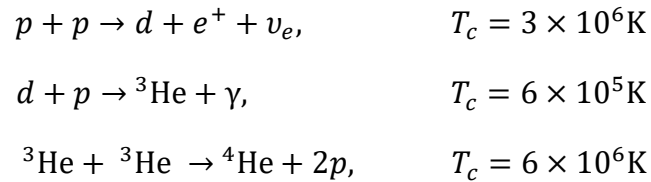
Figure 1 Evolution of the core temperature as predicted by Burrows et al. (1997) and shown by Burgasser (2002). Each line represents objects of masses 1, 5, 10, 13 (planets, “dot-dashed lines”) 20, 30, 42, 52, 63, 68, 75 (brown dwarfs, “solid line”) 80, 90, 100 M_J (stars, “dashed lines”). Also denoted are the lower limits for deuterium (T_D), lithium (T_L), and hydrogen fusion (T_H).

1.2.2 Internal Physics

A useful way to understand the internal physics of a brown dwarf is to examine them through the lens of stellar evolution. How do normal, hydrogen-burning stars form and what conclusions can be drawn from this about brown dwarf formation? Both pre-main-sequence stars and brown dwarfs follow standard formation theories (eg. Shu & Adams 1987) starting with the fragmentation and gravitational collapse of denser regions of cool, giant molecular clouds. This leads to the adiabatic contraction

of a protostellar object. As this protostellar object is compressed, its effective temperature will remain constant as shown through the Hayashi track (Hayashi 1961). Though the effective temperature remains constant, during this collapsing phase, the core temperature and core density will increase. The core temperature is proportional to the radius by the following relationship: $T_c \propto R^{-1}$ (Stahler 1988) if there is no accretion present. Figure 1 shows the temperature evolution of low mass objects (stars, brown dwarfs, and planets). Objects below the hydrogen burning mass will not sustain their temperature and, over time, cool. Those that achieve the critical mass for hydrogen fusion are able to sustain temperatures high enough for them to approach and enter as a main-sequence star.

For the contracting protostars with masses greater than the Hydrogen Burning Minimum Mass (HBMM), the central core will ultimately become hot enough to fuse hydrogen into helium. While other thermonuclear processes are important for nucleosynthesis, pp-I fusion chain (Hansen & Kawaler, 1994; Chabrier et al., 2000a) is how energy is generated for objects with brown dwarf like conditions.



This process provides 99% of the nuclear energy for objects with $M < 0.7M_\odot$ and releases a total of 26.7 MeV minus the energy carried away by the neutrino.

Fusion of hydrogen only will occur over a narrow range of temperatures. This is due to the influences of the Maxwell-Boltzmann thermal distribution ($\sim e^{E/kT}$) and quantum tunnelling ($\sim e^{b/E^{0.5}}$). The Maxwell-Boltzmann thermal distribution gives the number of particles at a particular energy, which decreases with energy. The quantum

tunnelling probability increases with energy. These opposing influences yield a strong Gamow energy peak which, according to Hansen & Kawaler (1994), is centered on $E_0 = 1.22(Z_1 Z_2 \mu T_6^2)^{\frac{1}{3}}$ keV. The Gamow peak, or the maximum probability of two nuclear particles overcoming the Coulomb Barrier to undergo nuclear reactions, is quite sensitive to temperature, which suggests that fusion becomes very efficient soon after the critical ignition temperature ($T_H \sim 3 \times 10^6$ K) is reached. The thermal and radiative pressures caused by hydrogen fusion then stop any further contraction of the protostar and hydrostatic equilibrium is thus achieved. It is at this point that a balance between energy generation in the core and radiative escape at the surface allow for this “new-born” star to approach and enter the Main-Sequence phase of its evolution.

One key indicator in brown dwarf evolution relates to electron degeneracy. For objects with lower masses, the core temperature and pressure increase at a slower rate during the period of contraction. This means that a higher density of material is needed to achieve the required temperature for fusion.

Electrons flowing in a plasma cannot be described by classical, point particles when the thermal deBroglie wavelength is comparable to the average interparticle distance Δx . This occurs in conditions with high densities and low temperatures. This occurs when the “degeneracy parameter” which Burrows & Liebert (1993) define as the ratio of the Fermi energy to the thermal energy is greater than unity (i.e., $\eta \gg 1$).

$$\eta \equiv \frac{E_F}{kT} = \frac{(3\pi^2 \hbar^3)^{\frac{2}{3}} \left[\frac{\rho N_A}{\mu_e} \right]^{\frac{2}{3}}}{2m_e kT} \cong 3.02 \times 10^5 T^{-1} \left[\frac{\rho}{\mu_e} \right]^{\frac{2}{3}} \quad (1.1)$$

Where E_F is the electron Fermi energy, and all other constants have their usual definitions. Stevenson (1991) and Burrows & Liebert (1993) show that the central core pressure is:

$$P_c = 10^{13} \left[\frac{\rho}{\mu_e} \right]^{\frac{5}{3}} \left[1 + \frac{\alpha}{\eta} \right] \text{ dyn/cm}^2 \quad (1.2)$$

Where $\alpha = \frac{5\mu_e}{2\mu}$. At large values for η , the pressure becomes adequate to stop further contraction of the protostar. If contraction is halted prior to the critical ignition temperature for hydrogen fusion, the resulting object is a brown dwarf.

Burrows & Liebert (1993) also derive an expression for the core temperature:

$$T_c = 2.06 \times 10^7 \left[\frac{M}{0.05M_\odot} \right]^{\frac{4}{3}} \left(\frac{\eta}{(\eta + \alpha)^2} \right) \text{ K} \quad (1.3)$$

From Equation (1.3), the core temperature is at a maximum when $\eta = \alpha$. So,

$$T_c^{max} = 3.43 \times 10^6 \left[\frac{M}{0.075M_\odot} \right]^{\frac{4}{3}} \text{ K} \quad (1.4)$$

This yields a HBMM of $0.068M_\odot$ for a hydrogen critical ignition temperature ($T_H \sim 3 \times 10^6$ K). More detailed models done by Burrows et al. (1997) and Chabrier & Baraffe (2000) calculate HBMM values ranging from $0.070M_\odot - 0.075M_\odot$ for objects with a Solar metallicity.

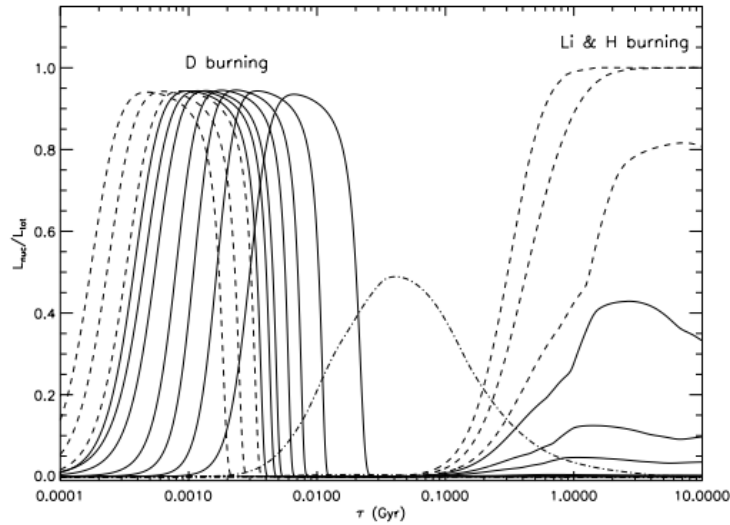


Figure 2 Evolution of the ratio of nuclear to total luminosity over time as predicted by Burrows et al. (1997) and shown by Burgasser (2002). The lines are the same as those of Figure 1.1. Regions of deuterium, lithium, and hydrogen burning are also noted.

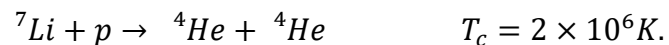
1.2.3 Fusion Processes in Brown Dwarfs

Both stars and brown dwarfs undergo deuterium fusion processes in their early lives. Figure 2 emphasizes this point by showing the contribution of luminosity from nuclear processes to the total luminosity of the object for a variety of differing masses. Similar to the HBMM defining the minimum mass for hydrogen fusion, deuterium also has a minimum burning mass. Grossman & Graboske (1973) find the Deuterium Burning Minimum Mass (DBMM) to be at $0.012M_{\odot}$ for an object with an age of $0.1 < \tau < 10$ Myr. During this time, 95% of the total emitted luminosity is generated by the second reaction in the pp-I chain ($d + p \rightarrow {}^3\text{He} + \gamma$). This reaction occurs at a

much faster rate than the pp-I chain due to the lower required temperature to fuse deuterium ($\sim 10^5$ K). This phase of deuterium burning does not last long since the abundance of this element is quite low. In fact, Piskunov et al. (1997) shows that for the local ISM, $D/H \approx 1.6 \times 10^{-5}$. This is significantly less than the relative abundance of hydrogen meaning that all the deuterium will be used up more quickly.

For objects less than the DBMM of $0.012M_{\odot}$, very little deuterium is burning leaving much of the initial deuterium “untouched.” The upper mass limit for brown dwarfs (boundary between brown dwarfs and hydrogen-burning stars) is quite clear as has been shown above. However, the lower mass limit is less obvious. The transition between “giant planets” and very low mass stars is vague. Shu, Adams, & Lizano (1987) propose that deuterium burning is a primary contributory factor in halting the accretion of matter onto a protostar. This implies that the lower mass limit for star formation occurs at the DBMM of $0.012M_{\odot}$. Objects less massive will not undergo any form of fusion thereby making them large planets. While the terminology of “giant planet” and “low-mass star” is still debated amongst the scientific community, all objects experiencing deuterium fusion will be identified as “low-mass brown dwarfs” in this paper for lack of confusion. For the most current IAU working definition of an exoplanet, see Lecavelier des Etangs & Lissauer (2022).

Another critical reaction that takes place in stars and some brown dwarfs is the fusion of lithium. The reaction occurs such that (Hansen & Kawaler 1994)



Chabrier & Baraffe (2000) suggest that lithium has been completely depleted within approximately 100 Myr. For stars less massive than $0.3M_{\odot}$, all the lithium (and similarly deuterium) present will be burned away. This occurs because at such low

masses, convective currents permeate the entire star. Material in the interior will cycle itself through the core since temperatures are low enough to allow for a convective-dominated mode of energy transport. Brown dwarfs are fully convective bodies. Stars with higher masses do not have convection cycles that penetrate the core suggesting that some interior material will be left “unburned” by fusion in the core. The presence of lithium remains important when searching for brown dwarfs because it implies that the object in question is both young and of low mass. Indeed, because the critical mass required for lithium burning is quite close to that of the HBMM, a so called “lithium test” has been proposed by Rebolo, Martín, & Magazzu (1992). By detecting the 6708 Å resonance line, the properties of these substellar dwarfs can be identified and therefore classified. The lithium test provides a good estimate for the mass and ages of such objects. The tracks of low-mass stars and brown dwarfs run very closely together in the luminosity versus effective temperature plane of the HR Diagram sometimes making them difficult to distinguish. Due to this proximity and the uncertainty in these tracks, the lithium test is a useful (yet not perfect) method to categorize brown dwarfs from low-mass stars. Figure 3 more clearly illustrates the temperature and age regions where lithium will be depleted and shows the region where the presence of lithium guarantees that the object is substellar. This test has been applied to several brown dwarf searches in clusters, in the field, and for stellar companions and serves as a useful tool, even today, for the detection of brown dwarfs.

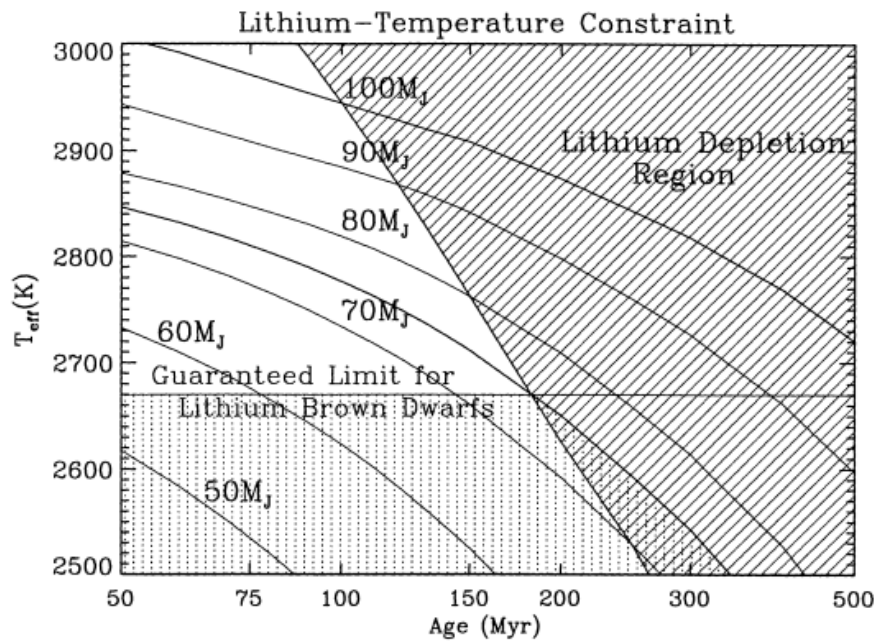


Figure 3 Illustration of evolutionary tracks for objects with different, indicated masses and how their effective temperatures relate to lithium depletion from Basri et al. (1998). The hatched region to the right of the plot shows where lithium is being depleted. The stippled region on the lower half of the indicates where the presence of lithium guarantees a substellar object regardless of age.

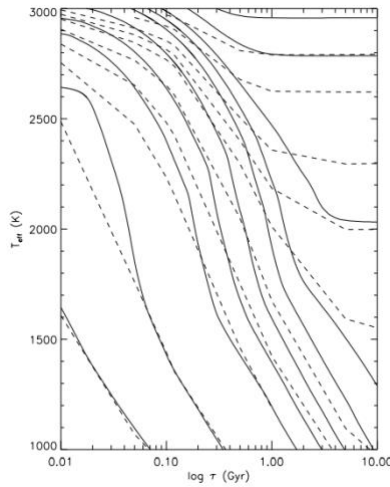


Figure 5 Evolution of effective temperature in low-mass dwarfs as predicted by Burrows et al. (1997, solid lines) & Chabrier et al. (2000a, dashed lines) and presented by Burgasser (2002). From left to right and bottom to top, the lines represent masses of 10, 20, 30, 40, 50, 60, 70, 75, 80, 90, and 100 M_{Jup} .

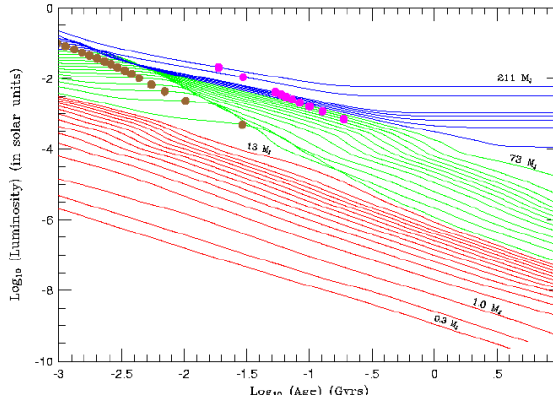


Figure 4 Evolution of luminosity for red dwarfs and substellar objects with solar metallicity from Burrows et al. (2001). Stars are denoted by blue lines, brown dwarfs above 13 M_{Jup} are denoted with green lines, and brown dwarfs/giant planets are given by red lines. The masses of these objects range from 0.3 M_{Jup} to 211 M_{Jup} (0.2 M_{\odot}). The brown dots show where 50% of available deuterium has been burned and the purple dots indicate where 50% of available lithium has been burned.

1.2.4 Life and Evolution

As with stars, the fate of brown dwarfs is predetermined by their initial mass and chemical composition. In a strictly evolutionary context, the same physics and chemistry can be applied to both types of objects.

Burrows et al. (2001) sums up brown dwarf evolution the best by saying that “they cool off inexorably like dying embers plucked from a fire.” This happens because the radiative losses are never adequately balanced by the compression of these degenerate objects. After an initial contraction phase, this imbalance between the radiation loss and compression leads to cooling of the central core temperature as shown in Figure 1. However, Figure 4 may demonstrate this effect more clearly by examining the evolution of effective temperature. Clearly, objects both above and below $70M_{\text{Jup}}$ can sustain temperatures similar to those of the coolest stars until roughly 300Myr. Around 1Gyr, though, these evolutionary tracks diverge such that objects $>70M_{\text{Jup}}$ settle onto the main sequence while those $<70M_{\text{Jup}}$ dwindle into oblivion. A similar pattern arises in the evolution of luminosity in low mass objects depicted in Figure 5. Objects with and without deuterium cool and dim quickly, regardless of their mass. However, objects without deuterium will cool and dim quicker than objects containing deuterium. The bifurcation between the blue and green tracks in Figure 5 further reinforce the idea that objects above the HBMM will settle onto the main sequence; not cool and fad as is done by objects below this critical

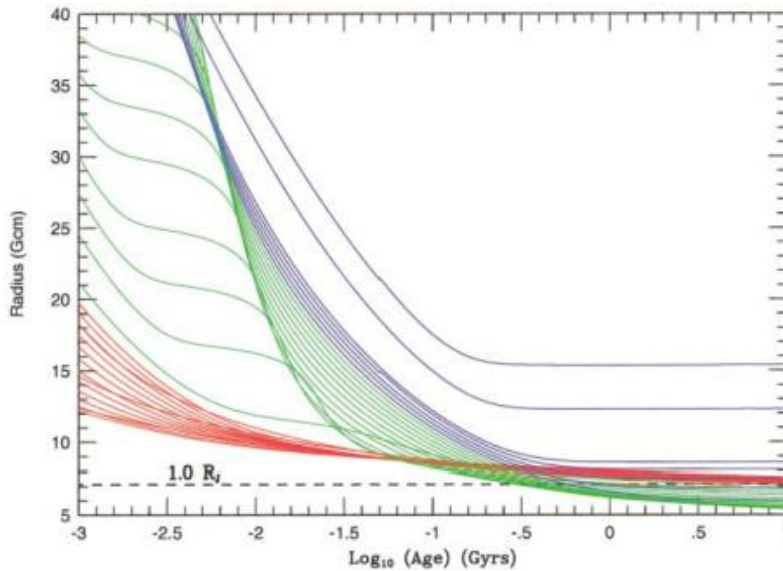


Figure 6 This figure taken from Burrows et al. (2001) shows the evolutionary tracks of substellar objects of different masses (lines and color schematic are the same as those of Figure 5). Also denoted is the radius of Jupiter. Note that the radii are not monotonic with mass and that they settle to values around that of R_{Jup} in later times, despite the wide range of masses represented.

mass. The minimum temperature and luminosity achieved by a star varies from model to model, as is evident in the discrepancy between the solid and dashed lines in Figure 4. These values are also heavily dependent on metallicity. But Burrows et al. (2001) has found that the minimum temperature and luminosity lies around 1700K and $6 \times 10^{-5} L_{\odot}$ respectively.

Unlike effective temperature, the radius of brown dwarfs does not evolve rapidly over time. At very early times, while brown dwarfs are burning their deuterium, contraction is stabilized due to the nuclear reactions occurring in the core. Once all the deuterium has been burned in the core, a phase of rapid contraction will

ensue. This compression causes the central temperature to increase, as shown in Figure 1 until electron degeneracy effects halt the collapse. Once brown dwarfs have completed their initial collapse, the radius stabilizes. This is evident in Figure 6 where, for later times, brown dwarfs settle to a radius within 30% of $1R_{Jup}$ where $1R_{Jup} = 7.15 \times 10^9 \text{cm}$ (Tholen, Tejfel, & Cox 2000), independent of their mass. This is a result of the competition between the Coulomb barrier and electron degeneracy effects. The Coulomb barrier identifies a fixed distance between particles, and thus, a fixed density. This leads to a relationship between radius and mass where $R \propto M^{\frac{1}{3}}$. However, matter that is electron degenerate has a mass-radius relation of $R \propto M^{-\frac{1}{3}}$ derived from the fact that degenerate interiors imply an equation of state $P \propto \rho^{\frac{5}{3}}$ leading to a polytropic index of $n=1.0$ (Chandrasekhar, 1939). These competing effects essentially cancel out causing the radius to remain constant over roughly two orders of magnitude of mass (Burrows et al. 1993, Marley et al. 1996).

Since brown dwarfs can be treated as quasi-polytropic, simple analytical expressions can be developed to relate key quantities that describe the fundamental properties of these objects. A number of different people including Burrows & Liebert (1993), Marley et al. (1996), Burrows et al. (2001), and later Auddy et al. (2016) have derived the following relations useful for first-order estimates of brown dwarf evolution.

$$L \sim 4 \times 10^{-5} L_{\odot} \left(\frac{t}{10^9 \text{yr}} \right)^{-1.3} \left(\frac{M}{0.05 M_{\odot}} \right)^{2.64} \left(\frac{\kappa_R}{10^{-2} \text{cm}^2 \text{gm}^{-1}} \right)^{0.35} \quad (1.5)$$

$$T_{eff} \sim 1550 \text{K} \left(\frac{t}{10^9 \text{yr}} \right)^{-0.32} \left(\frac{M}{0.05 M_{\odot}} \right)^{0.83} \left(\frac{\kappa_R}{10^{-2} \text{cm}^2 \text{gm}^{-1}} \right)^{0.088} \quad (1.6)$$

$$M \sim 35 M_{Jup} \left(\frac{g}{10^5 \text{cm s}^{-2}} \right)^{0.64} \left(\frac{T_{eff}}{1000 \text{K}} \right)^{0.23} \quad (1.7)$$

$$t \sim 1\text{Gyr} \left(\frac{g}{10^5 \text{cm s}^{-2}} \right)^{1.7} \left(\frac{T_{eff}}{1000\text{K}} \right)^{-2.8} \quad (1.8)$$

$$R \sim 0.94R_{Jup} \left(\frac{g}{10^5 \text{cm s}^{-2}} \right)^{-0.18} \left(\frac{T_{eff}}{1000\text{K}} \right)^{0.11} \quad (1.9)$$

One important aspect to these expressions (and all the figures thus far) is the fact that they only hold for objects with an equivalent solar composition. Metallicity, or the presence of elements heavier than helium, is crucially important in determining brown dwarf evolution because it affects the atmospheric opacity. Naturally, brown dwarfs with low metallicity will experience high radiative losses (larger luminosities) since the atmospheres are more transparent. In this case, the central core temperature must be higher in order to sustain hydrogen fusion, implying a higher HBMM. Indeed, Burrows & Liebert (1993) have found a HBMM of $90M_{Jup}$ for stars with zero-metallicity. The higher luminosities also suggest that these substellar objects evolve more rapidly. In general, the life and evolution of brown dwarfs have become more well known as numerous detailed searches have been conducted with increased capabilities of accurately measuring mass and composition.

1.2.5 Atmospheres

Another field of particular interest is the study of low-mass star and brown dwarf atmospheres. For stars on the main sequence, atmospheric information can be ascertained through the study of the photosphere, or the effective “surface,” and the region immediately above it. The same is true for brown dwarfs, though there are some fundamental differences. Their effective temperatures range from below that of M-Dwarfs down to as cold as planets (T and Y Dwarfs on the HR Diagram). The low temperatures and pressures (100-3000K and 0.1-10 bar respectively) within the upper

layers of brown dwarfs make it an ideal environment for producing molecules. Unlike their hotter, more massive counterparts found on the main sequence, brown dwarfs have cool enough temperatures and high enough densities for elements to combine into molecules, rather than exist as monatomic ions and neutral atoms. The presence of these complex molecules in the atmosphere is evident through their spectra.

To properly treat and model brown dwarf photospheres (and similarly, their atmospheres), a multitude of different aspects must be considered. At a minimum, chemical equilibrium abundances of atoms, molecules, and condensates must be included based off available thermochemical data. Such data is typically comprised of opacity tables for each species, proper treatment of dust/grain formation and condensation, and a self-consistent method for radiative transfer to derive a pressure-temperature profile. These profiles give insight into the atmospheric and therefore chemical evolution of brown dwarfs. Other areas of importance include cloud formation (which occurs below $\sim 2800\text{K}$), condensate precipitation or “rainout,” and atmospheric turbulence and convection. Additionally, thousands to billions of spectral lines from molecules found in brown dwarf atmospheres contribute to the opacity. This must be properly accounted for so as not to neglect line-broadening mechanisms. The management of such large opacity databases has become a business of its own (Hauschildt et al., 2001). The spectral energy distributions of brown dwarfs are also important, as they serve as constraints on models of their interiors (Baraffe et al., 1995) as well as comparisons to observational data.

Those who have conducted chemical equilibrium calculations, such as Fegley & Lodders (1996), have shown that the most abundant molecules in substellar atmospheres include H_2 , H_2O , CO , CH_4 , N_2 , NH_3 , and H_2S . By far, hydrogen, carbon,

and nitrogen are the most abundant elements found. For hotter brown dwarfs (and some M dwarfs), metal oxides (e.g., VO, TiO) have also been detected in the atmosphere. But in the cool temperature regime, these metal oxides are replaced by hydrides (e.g., FeH, CaH, MgH), and condensable materials (e.g., Fe, CaTiO₃). The “rainout” from these latter species further contribute to the chemical evolution of the atmospheres as first proposed by (Fegley & Lodders, 1996) in an analogy to Jovian observations. Some alkali metals (Na, K, Cs, Rb) are also prominent in spectra for L dwarfs as the opacity from heavy metals is lost (Kirkpatrick et al. 1999b; Burrows, Marley, & Sharp, 2000). At temperatures around 1400K, these alkali metals are separated into hydrides, hydroxides, and chlorides, which are subsequently depleted from the photosphere (Lodders, 1999). At cooler and cooler temperatures, other various transitions will occur. Between 1300K-1500K, the primary carbon-based molecule will switch from CO to CH₄. N₂ switches to NH₃ at roughly 700K, and at roughly 250K-300K, both NH₃ and H₂O will condense and “rain” out of the photosphere (Fegley & Lodders, 1996; Burrows & Sharp, 1999). By examining these transitions on a pressure-temperature profile, rough temperature estimates for brown dwarfs can be obtained.

In addition to atomic and molecular abundances in the atmosphere playing a key role in attaining brown dwarf properties, so also does the presence of dust. Dust grains act as an additional source of opacity and contribute to atomic and molecular depletion making them a crucial component of atmospheric modeling, especially for the coldest, lowest-mass brown dwarfs. The existence of these grains further complicates models. It would thus be incorrect to model the flux coming from a brown dwarf as a simple blackbody. Indeed, brown dwarf spectra show no evidence for a true

continuum so there is no real “benchmark” point for such a treatment. Also, non-gray atmospheric models must be used due to the wavelength dependence of such grains. Pioneering work by Allard (1990) and the work done on dust formation by Tsuji et al. (1996) and Lunine et al. (1989) have further improved the understanding of these ultra-cool atmospheres. To highlight this work, Chabrier & Baraffe (1997) present evolutionary calculations for low-mass objects with non-gray atmospheres and various metallicities using complete line lists for H₂O, the dominant source of opacity in the infrared spectrum of these substellar objects. The work conducted, especially by Allard and collaborators, provides key links that couple interior and atmospheric models which produce theoretical spectra that can then be used in the derivation of important observables such as magnitude and color.

1.3 Summary

This chapter has highlighted some of the important aspects and fundamentals of brown dwarf astronomy from which the subsequent chapters are based. More extensive and complete reviews can be found in, but not limited to, Burrows & Liebert (1993), Allard et al. (1997), Chabrier & Baraffe (2000), and Burrows et al. (2001). The past sixty years has seen significant advancements in both the theoretical and observational study of brown dwarfs. While much is known and understood about the interior physics, evolution, and energy distributions of these objects, there are still many details and questions that remain unanswered. Some of these still-developing fields of study include brown dwarf formation, low mass star formation efficacy, the contribution of substellar matter to overall galactic mass, convective processes in the photospheres of cool brown dwarfs, cloud formation and atmospheric “weather,” and the formation of planetary systems (especially those with giant, gas planets). Many of

these problems and gaps in the theory provided the inspiration for early brown dwarf searches and continue to be sources of motivation today.

The discovery of Teide I and Gliese 229B (Rebolo et al. 1995; Oppenheimer et al. 1995) launched a new era of brown dwarf searches that have continued to this day. The coupling of theory and observations have led to numerous breakthroughs, especially in the field of atmospheres and spectral analysis. One area that has been slow to gain traction is the study of brown dwarf and substellar luminosities and luminosity functions. With telescopes and imaging techniques becoming more sophisticated by the year, it is becoming easier to derive accurate luminosity functions, particularly with space-based telescopes like *GAIA*. The remainder of this thesis will focus on the study, derivation, analysis, and interpretation of such luminosity functions from *GAIA* photometric data.

Chapter 2

MODES OF ANALYSIS

2.1 Introduction

A large focus of the rest of this thesis will be to construct and analyze luminosity functions for a set of brown dwarf candidates using available *GAIA* data. This chapter is included to familiarize the reader with this procedure. In section 2.2, we give an overview of *GAIA*, its mission, methods of data collection, and the subsequent public data releases. Sections 2.3 and 2.4 comprise of discussions on Hertzsprung-Russell (H-R) Diagrams and tangential velocities obtained from *GAIA*'s Catalogue of Nearby Stars (GCNS) sample. These measurements are critical for detecting a viable set of brown dwarf candidates. Following this in section 2.5, we describe the luminosity function and how it is found. Finally, in section 2.6, we briefly summarize the key points covered in this chapter.

2.2 *GAIA*

Astrometry is the discipline in astronomy that is concerned with accurately studying and measuring the changing positions of celestial objects. It has had a long and rich history extending back even before the invention of the telescope itself. Since this time, the field of astrometry has grown and flourished as a result of humanity's ever-increasing instrumentational capabilities. Improved angular accuracy has been a key driving force behind the advancements in astrometric measurements. After the creation and refinement of the telescope, angular accuracy has become substantially

better. This has led to numerous important discoveries, most notably including stellar proper motion (Halley, 1717), stellar aberration (Bradley, 1727), and trigonometric stellar parallax (Bessel 1838; Henderson 1840; von Struve 1840).

However, obtaining parallaxes remained quite difficult due to the distorting effects of Earth's atmosphere. Not until the mid-1990s did this begin to change with the introduction of space-based telescopes. In 1997, the European Space Agency (ESA) launched the Hipparcos satellite that measured the absolute parallax with milli-arcsecond accuracy of as many as 117995 objects (ESA, 1997). The data obtained from the Hipparcos mission has influenced many areas of astronomy. In particular, advancements to the structure and evolution of stars as well as the motion of stars and stellar groups were made. Even some limited structure and dynamics calculations of the Milky Way were made using Hipparcos.

The ESA's astrometric successor to Hipparcos is the *GAIA* mission. Launched in 2013 to Earth's second Lagrange Point (L_2), *GAIA* is taking astrometric measurements of billions of objects with the main goal of mapping a three-dimensional spatial and velocity distribution of stars to determine their various astrophysical properties such as surface gravity and effective temperature (*GAIA* Collaboration et al. 2016). This will unlock information pertaining to the formation, structure, and evolution of the Milky Way Galaxy. The Milky Way contains a wide variety of stars, planets, interstellar gas and dust, and dark matter all of which move in orbits determined by the gravitational force derived from the total galactic mass. Understanding all these aspects in one comprehensible picture is the main aim of the *GAIA* mission (*GAIA* Collaboration et al. 2016).

To achieve this end, *GAIA* takes a large, representative sample of objects in the galaxy to an absolute G band limiting magnitude of +21. The ability to observe such dim objects in the optical range of the electromagnetic spectrum allows *GAIA* to meet its scientific goals of providing a more coherent picture of the complexities of our host galaxy. The primary focuses of *GAIA* during its 12-year predicted mission lifetime include but is not limited to studies of galactic structure, dynamics, and evolution, star formation history, stellar physics and evolution, stellar variability and distance scales, binaries and multi-star systems, exoplanets, the solar system, and the Local Group (*GAIA* Collaboration et al. 2016). Though it is not a direct objective of *GAIA*, the ability to measure out to magnitudes $\sim +20$ make it a great tool to spot and analyze potential brown dwarfs. These small, cool, and dim objects are only visible at very high optical magnitudes or at lower wavelengths such as the infrared range.

The act of taking astrometric measurements is quite complex. *GAIA*'s measurement procedure is derived from the global astrometry concept successfully demonstrated by Hipparcos. The astrometry scanning method (Lindgren & Bastian, 2011) requires a satellite to be slowly spinning and undergoing precession (one complete spin takes approximately 3 hours; one complete precession takes approximately 72 Earth days) in order to measure the crossing times of targets transiting the focal planes. These times represent one-dimensional stellar positions relative to the instrument axes. These positions are then usually compiled and added to large catalogues for further investigation. Lindgren & Bastian (2011) and *GAIA* Collaboration et al. (2016) provide a more detailed review of this method. This measurement-taking method was the primary force behind the overall design considerations for the spacecraft.

Perhaps the most vital part of the entire *GAIA* mission is the functionality of the payload module. The payload module has three scientific purposes: astrometry, spectroscopy, and photometry. The payload module provides support for the two onboard telescopes. These include two, identical three-mirror reflector telescopes with apertures of 1.45m and focal lengths of 35m pointing in directions separated by an angle of 106.5° (*GAIA* Collaboration et al. 2016). This allows *GAIA* to view a large area of the sky at once while still maintaining the required spatial accuracy to measure very dim and distant objects. In fact, *GAIA* has a spatial resolution of down to 20-200 microarcsec. The high accuracy of *GAIA* also allows it to keep high spatial resolutions, magnitudes, and velocities at low magnitudes. For example, at a magnitude $M=+15$, *GAIA* maintains a spatial resolution of $10\mu\text{as}$, magnitude accuracy of 5mmag, and velocity accuracy down to 1km/s.

After the data has been collected and stored, it needs to be processed and analyzed to produce scientifically meaningful quantities. This falls under the purview of the *GAIA* Data Processing and Analysis Consortium (DPAC), which was formally started in 2006 and consists of over 450 active astronomers, software engineers, and project management specialists.

The *GAIA* data processing method is a very complex task that serves a host of different scientific goals. *GAIA* Collaboration et al. (2016) breaks the processing procedures down into two broad categories: daily and cyclic. The daily assignments consist of producing the preprocessed data needed for the cyclic systems, providing near-real time system health updates, and providing data to feed the alert systems. On the other hand, the cyclic tasks switch between calibration and the determination of source parameters (*GAIA* Collaboration et al. 2016). A brief list of the daily processing

tasks is provided here: initial data treatment, astrometric verification, science alerts, and solar system alerts. The cyclic processing tasks include intermediate data updates, astrometric global iterative solutions, global sphere reconstruction, and photometric pipelines. These tasks aim to update basic calibrations, reprocess all the latest raw observations, and provide improved astrometric, photometric, and spectroscopic measurements for each source. *GAIA* Collaboration et al. (2016) also provides an overview of further cyclic processes used for more advanced data analysis.

As a result of these daily and cyclic processing tasks, raw data is reprocessed, collected, and prepared for release in such a way that it is meaningful for the scientific community and the public at large. After DPAC processes, calibrates, and validates the data, it is released to the world without limitations in the form of public data releases. Since the *GAIA* mission has no data rights, anyone may access the data from these releases and perform a wide variety of scientific studies. Three main data releases have occurred thus far with several intermediate releases roughly occurring every year. This thesis makes use of the *GAIA* Early Data Release 3 (EDR3) released in 2020. *GAIA* EDR3 contains astrometry and photometry for 1.8 billion sources brighter than a G band magnitude of +21. It also includes celestial positions and apparent G-band magnitudes for each of these sources. For approximately 1.5 billion of these sources, parallaxes, proper motions, and colors are available (*GAIA* Collaboration et al. 2020). Specifically, to calculate the luminosity functions for brown dwarf candidates, this thesis makes use of the *GAIA* Catalogue of Nearby Stars (GCNS), a subset of EDR3, which includes over 300000 objects within 100pc of the Sun (*GAIA* Collaboration et al. 2021). GCNS provides a great, up-to-date catalogue of

nearby objects to a high degree of accuracy that can be analyzed to ascertain information about elusive brown dwarfs.

This section provides but an overview of *GAIA*, its mission, and how it collects, stores, processes, and releases its data. *GAIA* Collaboration et al. (2016) provides a more in-depth review of the material covered here.

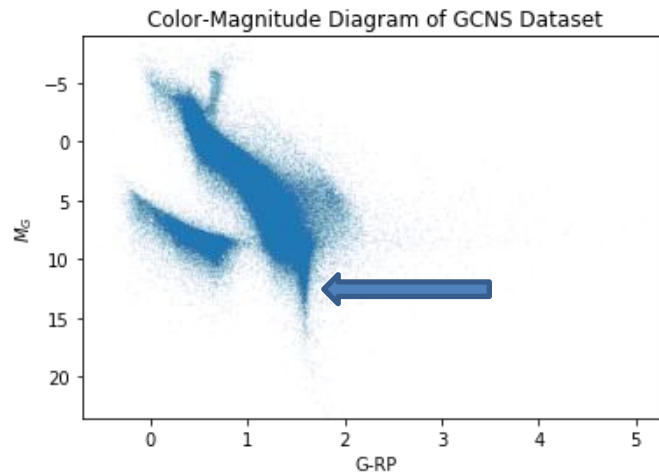


Figure 7 Color-Magnitude Diagram of GCNS data using G-RP color index and absolute magnitude in the G band. This figure clearly shows the location of the main sequence (high density region going from top left to bottom right). Also depicted in this figure is the Red Giant Branch turnoff (outcropping located at the top of the main sequence). For reference, the sun would lie near the center of the main sequence. Potential brown dwarfs would lie in and around the tail extending from the

2.3 Color-Magnitude Diagram

GAIA's public data releases contain a plethora of information on well over 1 billion stars. EDR3 is no exception to this. As has been described above, EDR3 contains astrometric and photometric data including parallaxes, proper motions, and magnitudes using various filters (e.g., G band and J band). Being a subset of EDR3, GCNS contains this same information, which is more than enough to obtain the crucial Color-Magnitude Diagram. The Color-Magnitude diagram is a vital tool that astronomers use to ascertain various astrophysical properties of stars. For example, color-magnitude diagrams can indicate an object's magnitude and brightness. For the

purposes of this thesis, stellar magnitude and color data were used to create the color-magnitude diagram shown in Figure 7.

GCNS does not include absolute magnitudes, but they were trivially calculated in the G band using the distance modulus formula since distances and apparent magnitudes were provided.

$$M_G = m_G - 5 \log\left(\frac{d}{10 \text{ pc}}\right) \quad (2.1)$$

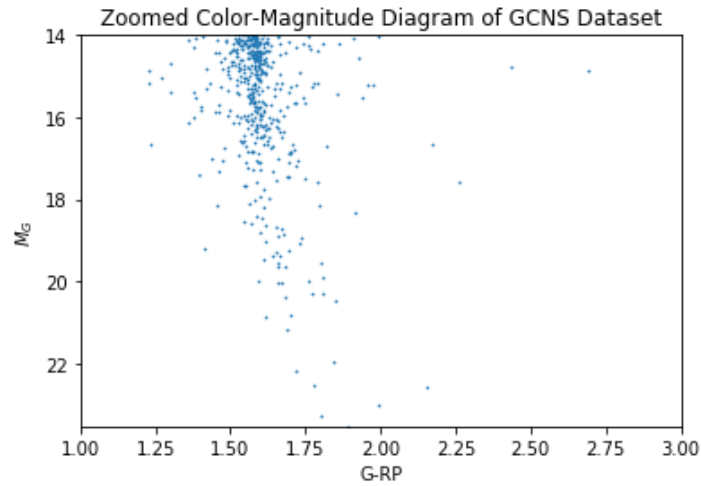


Figure 8 Color-Magnitude Diagram of Figure 7 zoomed in on the bottom tail of the main sequence where potential brown dwarfs would reside.

The color index was also easily found by taking the difference between the G band magnitude and RP band magnitude (e.g., G-RP). Effects of reddening and extinction need not be accounted for due to the fact that this sample only includes the solar neighborhood out to 100pc.

The main reason for creating this color-magnitude diagram is to constrain the GCNS sample by limiting the absolute magnitude and color. Since brown dwarfs are known to be cool and thereby quite dim (high magnitudes) in the optical range, it can be reasonably assumed that any potential brown dwarf candidates would likely be located near the bottom end of the main sequence. This region is clearly indicated in Figure 7 as the vertical tail extending downwards to dimmer absolute magnitudes. Figure 8 zooms in on this region of Figure 7 so one can better visualize this sample of objects.

Using Figure 8, the absolute G band magnitudes were constrained to values between $M_G=14.0$ and the maximum magnitude (dimmiest object) detected in the sample, while the color index was constrained to $G-RP=1.0$ to $G-RP=3.0$.

The color-magnitude diagram is a great tool for selecting brown dwarf candidates since their location on it is generally well-defined. The brown dwarf upper limit is especially well established since the HBMM is known to be at roughly $0.07M_{\odot}$. This corresponds to a specific location on the color-magnitude diagram where below, brown dwarfs and other “failed stars” reside and evolve. For reference, the L0 spectral type (effective boundary between type M red dwarfs and type L brown dwarfs) corresponds to $M_G = +16.4$. With the ultimate goal of creating luminosity functions for brown dwarf candidates, obtaining these magnitude and color constraints from the color-magnitude diagram is a critical first step in visualizing and understanding which stars will be included and which will be rejected.

The next section will examine tangential velocity constraints that were also used to further limit the GCNS dataset to a viable subset of brown dwarf candidates.

2.4 Tangential Velocities

In addition to H-R diagrams, the GCNS dataset also allows for the calculation of tangential velocities. Tangential velocity measures the linear speed of an object as it travels across the plane of the sky. Tangential velocity is but a component of the true space velocity of an object. In order to calculate an object's true velocity through space, both tangential velocity and radial velocity components must be included.

Tangential velocity is defined as:

$$v_t = 4.74\mu d \quad (2.2)$$

where μ is the proper motion in arcsec/yr, and d is the distance to the object in parsecs. This yields a velocity with units of km/sec.

To get the true space velocity, simply take the sum of the tangential velocity, v_t , and the radial velocity, v_r , (found by using the Doppler shift of its spectrum) components and use kinematics.

$$v_{true}^2 = \sqrt{v_r^2 + v_t^2} \quad (2.3)$$

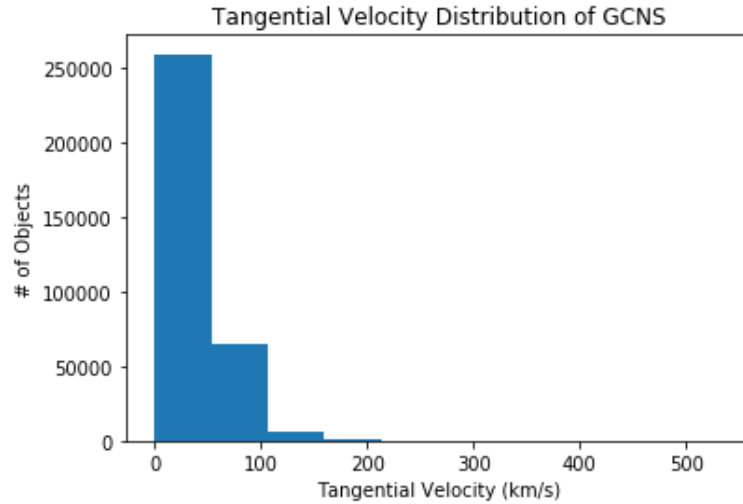


Figure 9 Shows a histogram of tangential velocities for all stars in GCNS with $0.0 < M_G < 20.0$. Most stars in the sample have tangential velocities less than 50km/s.

However, the tangential velocity alone reveals much about an object, including a statistical age. To understand this, consider the process of star formation from giant molecular clouds. Protostellar gas clouds typically move in a circular orbit in the galactic plane with little to no tangential velocities. In fact, several studies including Dickey, Salpeter, & Terzian (1978) and Crovisier (1978) have found that HI clouds of a few M_\odot to have velocity dispersions $\sigma_v \approx 5 - 11 \text{ km sec}^{-1}$, while giant molecular clouds 10^4 times more massive have $\sigma_v \approx 6.6 \text{ km sec}^{-1}$. This suggests a mean velocity dispersion of around 9 km sec^{-1} . With these clouds having very small eccentricities, the stars formed within them will also have a highly circular galactic orbit and have small tangential velocities. Over time though, the protostellar cloud and the stars within it will gravitationally interact with external objects such as other

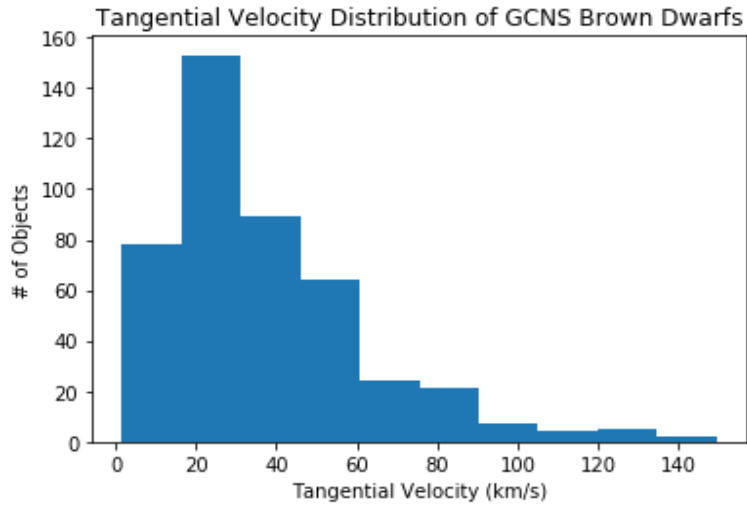


Figure 10 Histogram of a subset of GCNS with $14.0 < M_G < 20.0$ and $1.0 < G - RP < 3.0$ magnitude and color constraints. This subset encompasses brown dwarf candidates. It is easily seen that most stars in this sample have tangential velocities between 20-40km/s.

protostellar gas clouds or even galaxies during a galactic collision or merger. Such large-scale interactions disturb the highly circular galactic orbits of stars within these star-forming regions and can send them off with highly irregular trajectories. By using this tangential velocity information, a statistical age for these stars can be determined. Younger stars tend to have smaller v_t values since they have not undergone as many gravitational interactions to disrupt their highly circular orbits. Older stars usually have larger v_t values since their orbits have been more disturbed over time. Of course, this is not always true for every individual star. Stars must be examined on a case-by-case basis to truly determine their age, but statistically speaking this relationship between v_t and age generally holds.

Using Equation (2.2) and the distance and proper motion information from GCNS, Figure 9 shows a histogram of v_t for stars with absolute magnitudes $0.0 < M_G < 20.0$. Most stars in Figure 9 have tangential velocities below 50 km sec^{-1} while substantially less are greater than 100 km sec^{-1} . An initial assessment would suggest that most stars in the sample are relatively young. Figure 10 takes a subset of objects from GCNS and shows their tangential velocity distribution in histogram format. For this figure, the constraints applied are $14.0 < M_G < 20.0$ and $1.0 < G - RP < 3.0$. This sample of objects includes brown dwarf candidates. Most of the objects have velocities ranging from $20.0 < v_t < 40.0 \text{ km sec}^{-1}$. Figure 9 helps determine that most stars in GCNS are young since the tangential velocity distribution peaks below 50 km sec^{-1} . Figure 10 extends this hypothesis to the brown dwarf regime for the same reason.

With the color-magnitude diagram and tangential velocities of the brown dwarf subset of GCNS in place, it will now be beneficial to discuss the luminosity function and the procedure used to calculate it.

2.5 The Luminosity Function

The GCNS is a superb dataset from which the local luminosity function can be derived. Generally, the luminosity function is used to obtain the number of stars or galaxies per a luminosity or magnitude interval. This is possible by using volume-limited samples and parallaxes not derived from photometric measurements that includes biases, but rather from astrometric measurements (*GAIA* Collaboration et al. 2021). This section discusses the procedure followed to obtain the luminosity functions of the GCNS dataset and a subset of brown dwarfs.

The stellar luminosity function is generally defined as (Tinney et al. 1993):

$$\Phi(M_i)dM_i = \frac{n_\star}{\text{pc}^3} dM_i \quad (2.4)$$

where n_\star is the number of stars in the sample, M_i is a given absolute magnitude (i.e. M_G), and dM_i is the absolute magnitude bin width.

For both the GCNS and subsequently the brown dwarf luminosity functions, a classical technique of using a generalized form of the maximum volume V_{max} (Schmidt, 1968) was used to calculate Φ . For a given absolute magnitude in the G band (M_G), the maximum probed volume was calculated. Additionally, Felten (1976) and Tinney et al. (1993) correct this classical technique to account for a decreasing stellar density as distance above or below the galactic plane increases. The expression for V_{max} is thus:

$$V_{max} = \Omega \frac{H^3}{\sin^3 |b|} [2 - (\xi^2 + 2\xi + 2) \exp(-\xi)] \quad (2.5)$$

with

$$\xi = \frac{d_{max} \sin |b|}{H} \quad (2.6)$$

where H is the thin-disc scale height and d_{max} is the maximum distance of detection. b and Ω are the Galactic latitude and the area of the sky to which the star belongs respectively. Ω was estimated to be 4π since *GAIA* maps the entire sky from its location in space. H was assumed to be 365pc as derived by *GAIA* Collaboration et al. (2021).

The value for the maximum probed distance d_{max} was estimated for each object in the sample using a variation of the distance modulus found in Equation (2.1) thereby making it the inverse of the maximum volume V_{max} in which it was observed (*GAIA* Collaboration et al. 2021). The value for d_{max} was capped at 100pc to further

limit any uncertainties in the calculations. So, d_{max} had a value between 0pc and 100pc for each object. Thus, the luminosity function of Equation (2.4) can be recast into terms of V_{max} as the sum over all objects found within an absolute magnitude bin:

$$\Phi(M_i) = \sum \frac{1}{V_{max}} \quad (2.7)$$

Using this in conjunction with Equation (2.6), luminosity functions were thus obtained for GCNS and a subset of brown dwarfs.

Specifically, only a constraint on M_G was applied to determine the luminosity function of the overall GCNS set. This constraint limited M_G to $0.0 < M_G < +20.0$ but still encompasses over 99% of the sample. However, to get an accurate luminosity function for the subset of brown dwarfs, more constraints were needed. In addition to M_G constraints, limiting color indices and tangential velocities were added. To only include brown dwarfs, the M_G constraint that was applied further limited the sample to stars of $14.0 < M_G < 20.0$ (ranging from M6-L8 spectral type). The color constraint limited $G-G_{RP}$ to $1.0 < G - G_{RP} < 3.0$ which was found using the color-magnitude diagram in Fig. 8. The tangential velocity was divided into two categories: (1) $v_t \leq 20 \frac{\text{km}}{\text{s}}$ and (2) $v_t \geq 100 \frac{\text{km}}{\text{s}}$. Having these constraints which identifies the slow-moving and fast-moving stars will give insight into how they behave as they age.

Confidence intervals and error measurements also needed to be accounted for in the calculation of the luminosity function. As M_G increases, *GAIA* will produce more uncertain measurements since it is detecting fewer objects at such high magnitudes in optical wavelengths. To calculate this confidence interval, the luminosity function was related to the number of objects within each absolute magnitude bin such that:

$$confidence = \pm \frac{\Phi}{\sqrt{bincount}} \quad (2.8)$$

where *bincount* is defined as the number of objects found within each absolute magnitude bin.

Now that a method for calculating and obtaining the luminosity function has been examined, the next chapter will present and discuss these results for the GCNS dataset generally and for a limited set of brown dwarf candidates within this catalogue.

2.6 Summary

This chapter has examined the *GAIA* spacecraft and mission and how it has been and will continue to be used in the pursuit of gaining a more complete picture of the formation, structure, and evolution of the Milky Way. In addition to cataloguing extremely precise astrometric measurements of over 1 billion stars in the three data releases since the start of the mission, *GAIA* has propelled many subfields in astronomy forward with its direct detection of exoplanets, star clusters and star forming regions, and not least of all, the detection of previously undiscovered faint objects such as potential brown dwarfs.

In its most recent release to date, the *GAIA* Early Data Release 3 (EDR3), *GAIA* also released a dataset of nearby stars, the *GAIA* Catalogue of Nearby Stars (GCNS). The GCNS has precise astrometric measurements for well over 300,000 objects within a 100pc radius of the Sun. This makes it a great dataset for deriving and measuring the local stellar luminosity function with high accuracy down to very faint absolute magnitudes ($M_G \sim 20.0$). To obtain the luminosity function, only M_G and d_{max} needed to be found as explained in detail by Tinney et al. (1993). All other quantities used in the generalized V_{max} technique first used by Schmidt (1968) were found

directly from GCNS itself. However, to find the luminosity function for a set of brown dwarfs within GCNS, additional constraints needed to be applied which included tangential velocity v_t and color (G-G_{RP}) constraints. The limiting values for M_G and color were found by creating and analyzing an H-R diagram of GCNS and selecting the magnitude and color range in which brown dwarfs typically reside. v_t was divided into two categories with low v_t values representing younger objects and high v_t values representing older objects.

With the procedure for calculating the luminosity function and adding constraints in place, the next chapter will examine the resulting luminosity functions of GCNS and a subset of brown dwarfs and discuss their significance.

Chapter 3

RESULTS

3.1 Introduction

The following chapter will highlight the resulting luminosity function obtained through the procedure described in Chapter 2 and how it compares to accepted models. In section 3.2, the luminosity function is presented and interpreted for the reader. Section 3.3 outlines the analytical brown dwarf and low mass stellar models used for comparisons to the *GAIA* luminosity function. Specifically, subsection 3.3.1 will cover the Sonora atmosphere and brown dwarf models produced by Marley et al. (2021). In subsection 3.3.2, models from Fernandes et al. (2019) are introduced and discussed. Subsection 3.3.3 discusses the combination of the models from Marley et al. (2021) and Fernandes et al. (2019) for the purposes of obtaining a more complete model. Following this in subsection 3.3.4, the *GAIA* data is cross matched with models from Filippazzo et al. (2015) with the goal of developing a relationship between absolute bolometric magnitude and the absolute *GAIA* magnitude in the G band. In section 3.4, the model data is compared to the observational data obtained from *GAIA*. Finally, in section 3.5, we review the main results and interpretations discussed in this chapter.

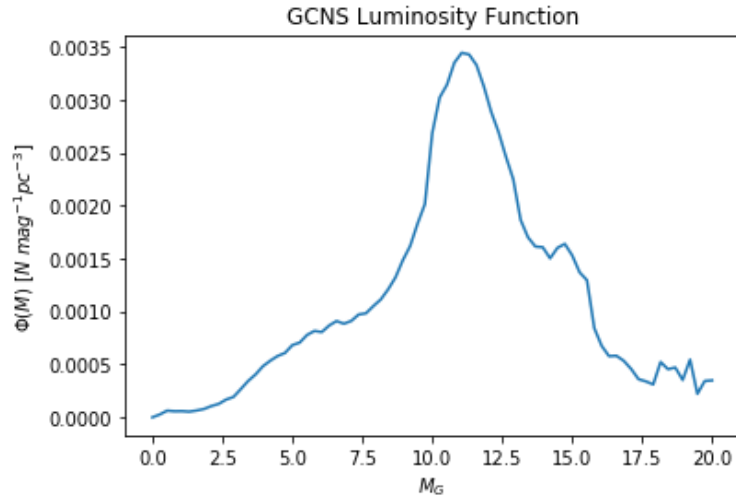


Figure 11 This figure shows the luminosity function of the GCNS sample computed for absolute *GAIA* magnitudes $0.0 < M_G < +20.0$ counted in 0.25 magnitude bins on a linear scale. A noticeable peak occurs around $M_G \approx +11.0$.

3.2 *GAIA* Luminosity Functions

With the procedure outlined in chapter 2 using the method presented in *GAIA* Collaboration et al. (2021), luminosity functions of the GCNS sample were obtained. From the classical V_{max} technique first introduced by Schmidt (1968), expressions for V_{max} and $\Phi(M_i)$ are found and highlighted in Eqns. 2.5, 2.6, and 2.7. Using these formulae on the GCNS sample, a space density was constructed for a sequence of absolute *GAIA* G-band magnitude intervals. Figure 11 shows this luminosity function with 0.25 magnitude bins ranging from $0.0 < M_G < +20.0$. There is a noticeable peak around $M_G \approx +12.0$ where $\Phi \approx 3.5 \times 10^{-3}$ stars mag $^{-1}$ pc $^{-3}$. This corresponds roughly to the M3 spectral type stars. Following this peak, the luminosity function then dips as it approaches the HBMM boundary.

Figure 11 corroborates the work done in *GAIA* Collaboration et al. (2021) quite well as the figure from this study also has a similar structure with an obvious peak around the same M_G values. However, the main goal of this thesis is to investigate the luminosity function specifically for brown dwarfs around the stellar/substellar boundary.

With this goal in mind, additional constraints were applied to narrow the sample size. As discussed in section 2.3 and shown in Figure 8, a color index constraint ($1.00 < G - RP < 3.00$) was applied to only include the low end of the main sequence and beyond. An additional magnitude (M_G) constraint was added as well to only include objects with $+14.0 < M_G < +20.0$. Again, the L0 spectral type which corresponds to a mass just below the HBMM lies at $M_G = +16.4$ makes this range of M_G values ideal for investigating this boundary. The measurements were capped at $M_G = +20.0$ due to *GAIA*'s G magnitude limitations.

Recall from section 2.4 that tangential velocity can also provide insight into stars and brown dwarfs. Objects with high tangential velocities are generally older than their counterparts with low velocities since they have had more time for their orbits to become perturbed due to external gravitational influences. Therefore, two cases were studied. In one case, the luminosity function for slow moving, younger objects was studied. The other case investigated the luminosity function for faster, older objects. Figure 12 shows these two luminosity functions normalized to each other's peak value and overplotted with one another with an estimated error defined in Equation (2.8).

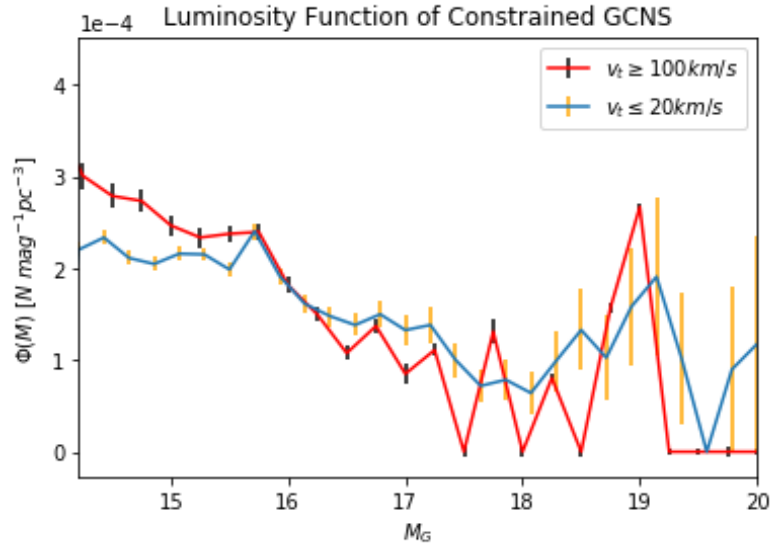


Figure 12 This figure shows the luminosity functions of the constrained GCNS sample for objects with $v_t \leq 20\text{km/s}$ (blue curve) and $v_t \geq 100\text{km/s}$ (red curve) with the aforementioned color and magnitude constraints (i.e. $1.00 < G - RP < 3.00$ and $+14.0 < M_G < +20.0$) and separate into 0.25 magnitude bins. The functions have been normalized to each other in order to overplot them. In both cases, the luminosity function steadily decreases as magnitude increases.

In Figure 12, both curves start around $\Phi \approx 3.0 \times 10^{-4}$ stars $\text{mag}^{-1}\text{pc}^{-3}$ and subsequently decrease for higher and higher magnitudes. This suggests that most objects within the constrained GCNS sample lie at brighter magnitudes. Intuitively, this should make sense since *GAIA* collects data in the optical wavelengths meaning it should detect more bright objects than dim objects, faint objects. Indeed, as the *GAIA* G-band magnitude increases, it identifies fewer objects per cubic parsec which therefore leads to a drop in the luminosity function. It is for this reason that the confidence interval or error values increase as the limiting G magnitude approaches.

GAIA is detecting fewer objects for a given magnitude bin leading to a greater uncertainty at higher values of M_G .

In this section the luminosity functions for young and old objects are presented from the constrained GCNS sample. Figure 12 shows that *GAIA* is a great source for measuring these luminosity functions to a high degree of confidence even out to quite dim absolute magnitudes. Approaching *GAIA*'s limiting G band magnitude of $M_G = +20.4$ (i.e. $M_G > +18.5$) does cause an increase in uncertainty due to fewer objects being discovered within a given magnitude bin. But what do these luminosity functions reveal? How does one know if there are truly brown dwarfs in this sample? To better contextualize Figure 12, it would be useful to compare *GAIA*'s observational data to accepted brown dwarf models. The following section will introduce the theoretical models used in the comparison.

3.3 Theoretical Brown Dwarf Models

With the *GAIA* luminosity functions for young and old brown dwarf candidates firmly in place, it would be useful to interpret them through a comparison with various accepted brown dwarf and low stellar mass models. Making these comparisons will shed light into the nature of the luminosity functions and give insight into the type of objects *GAIA* is detecting and their underlying physical processes. The following subsections will introduce models from Marley et al. (2021), Fernandes et al. (2019), and Filippazzo et al. (2015) that describe brown dwarf and low mass stellar properties.

3.3.1 Sonora Substellar Models

The first set of models come from Marley et al. (2021) where they were applied to cloudless atmospheres of substellar L, Y, and T dwarfs as well as self-

luminous extra-solar planets. The models are given the moniker “Sonora” after the Sonora desert located in the southwestern United States and northern Mexico. Specifically, these Sonora models contain improved opacity and atmospheric chemistry measurements for use in the study of brown dwarf and exo-planet atmospheres. These updated atmospheric and evolutionary tables provide the temperature-pressure profiles and emergent spectra for objects with temperatures, gravities, and masses ranging from $200 \leq T_{eff} \leq 2400$ K, $2.5 \leq \log g \leq 5.5$, and 0.5 to 85 Jovian masses respectively. The models also address how these characteristics change with metallicity (i.e. $[M/H]=-0.5$ - $+0.5$). Another key feature in the evolutionary tables is that they describe the cooling of these substellar objects over time.

For the purposes of this analysis, the models containing 10Gyr objects for metal-poor ($[M/H]=-0.5$) and metal-rich objects ($[M/H]=+0.0$, i.e. solar metallicity) were used. To ensure a proper comparison to the brown dwarf candidates suggested through the *GAIA* analysis, it is necessary to use the oldest provided 10Gyr models. The old models are used to confirm that the objects are in question are indeed brown dwarfs due to the stark evolutionary differences between stars and brown dwarfs at this late age. Since the selected model objects are old, it implies that their properties could be compared to the old brown dwarf candidates found using the GCNS sample to a high degree of confidence. Extracting the old objects from the GCNS sample and models ensures that they are more likely to be cool brown dwarfs rather than stars that lie above the HBMM due to the differences in evolutionary tracks outlined in Chapter 1.

The Sonora models are one of the more recent and up-to-date models describing objects in the substellar and planetary regimes. The parameters of these models make them optimal for investigating brown dwarfs and comparing them to observational data. However, one major limitation in the models is the upper mass limit. The Sonora models from Marley et al. (2021) have an upper mass of 85 Jovian masses, or $0.083M_{\odot}$. While this is perfectly fine for investigating the brown dwarf regime, it also is important to inspect the stellar regime just above the HBMM to guarantee a more complete comparison. In order to obtain a better understanding of the objects both above and below the HBMM, another model will need to be used to “extend” the Sonora models deeper into the stellar regime.

3.3.2 CLES Stellar Models

The next set of models that were used come from Fernandes et al. (2019). These models aim to better map out the ultra-cool dwarf regime. In the context of Fernandes et al. (2019), stellar and substellar models were constructed to obtain precise estimates of host parameters, which in turn constrain the physical properties of orbiting exo-planets. The fundamental parameters included in the Fernandes et al. (2019) models that are important in this thesis include mass, age, metallicity, and temperature. Similar to the Sonora models, here two models with an age of 10Gyr were extracted. One model was metal-poor with an iron to hydrogen ratio of -0.4 (i.e. $[\text{Fe}/\text{H}]=-0.4$). The other model had solar metallicity ($[\text{Fe}/\text{H}]=+0.0$). The key difference between the models presented by Fernandes et al. (2019) and Marley et al. (2021) is the mass and temperature ranges. Unlike the Sonora models that extend well into the substellar regime and are roughly limited by the HBMM, the Fernandes et al. (2019) models include higher masses and temperatures that correspond to stars on the main

sequence. The mass and temperature ranges for the Fernandes et al. (2019) models of interest are $0.085M_{\odot} - 0.13M_{\odot}$ and $\sim 2500 < T_{eff} < \sim 3000$ K respectively.

Though these masses and temperatures are indicative of main sequence stars that are fusing hydrogen, it is still of interest to use in the comparison to the observational data from *GAIA*. The constrained GCNS sample should include both

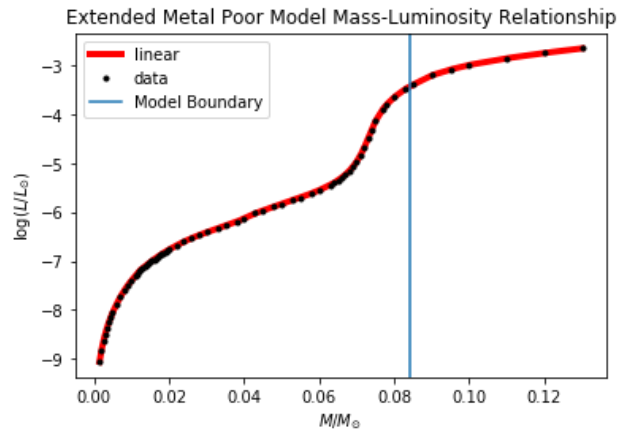


Figure 13 This figure shows the mass-luminosity relationship for the combined metal-poor models from Marley et al. (2021) and Fernandes et al. (2019). The mass ratio ranges from 0.015-0.013. The data was linearly interpolated for 1000 masses to provide a smooth relationship. The increase in luminosity around the mass ratio of 0.07 indicates that the HBMM lies at this point. Also note that there is no discontinuity between the two models due to the slight metallicity difference.

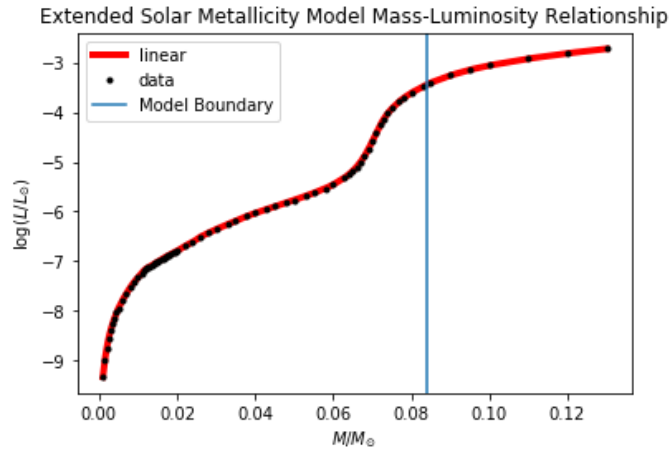


Figure 14 This figure shows the mass-luminosity relationship for the combined solar metallicity models from Marley et al. (2021) and Fernandes et al. (2019). Again, the mass ratio ranges from 0.015-0.13 and was linearly interpolated for 1000 masses. An increase still occurs around $0.07 \frac{M}{M_{\odot}}$ corresponding to the onset of nuclear fusion but is not as pronounced as in the metal-poor model.

brown dwarfs and stellar objects, so it is important to understand the behavior of both types of objects around the HBMM.

3.3.3 Combining the Models

The two models introduced in sections 3.3.1 and 3.3.2 provide valuable information into the properties of objects in both the stellar and substellar regimes surrounding the HBMM. With this in mind, it would be useful to combine the models for both metallicity constraints so a wider range of masses can be covered. This combination was done by using the Sonora models out to their maximum mass of $0.084M_{\odot}$ then cropping the CLES stellar models to only include masses from $0.084M_{\odot} - 0.13M_{\odot}$.

After combining the models, the new mass range now covers $0.015M_{\odot}$ – $0.13M_{\odot}$. This ranges from Y dwarfs up to type M stars, perfect for investigating the hydrogen burning limit of roughly $0.075M_{\odot}$ (HBMM changes slightly based on metallicity). One small difference between the Sonora models and the models from Fernandes et al. (2019) that should be noted is the metallicity difference for the metal-poor models. The Sonora metal-poor model has a metallicity ratio of -0.5 while the Fernandes et al. (2019) metal-poor model has a metallicity ratio of -0.4. Though there is a slight difference between the two, it does not cause any discontinuities in the extended model results as emphasized in the mass-luminosity and mass-temperature relationships shown in Figures 13-16.

The relationship between mass and luminosity is vital to understanding the differences between main sequence stars and brown dwarfs. Realizing how they differ sheds light into the different physical processes that occur in objects above and below the HBMM. Figure 13 and Figure 14 show linearly interpolated mass-luminosity relationships for the combined metal-poor and solar metallicity models for 1000 masses between $0.01M_{\odot}$ and $0.13M_{\odot}$. In both Figure 13 and Figure 14, there is a sharp increase in luminosity at low masses that corresponds to the onset of

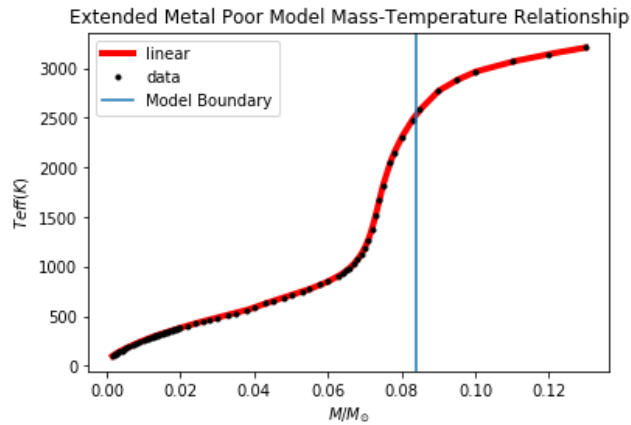


Figure 15 This figure shows the linearly interpolated mass-temperature relationship for 1000 masses between $0.01M_{\odot}$ and $0.13M_{\odot}$. The data comes from the combined metal-poor models from Marley et al. (2021) and Fernandes et al. (2019). There is a dramatic increase in temperature around the HBMM. At low and high masses, though, the temperature only gradually increases.

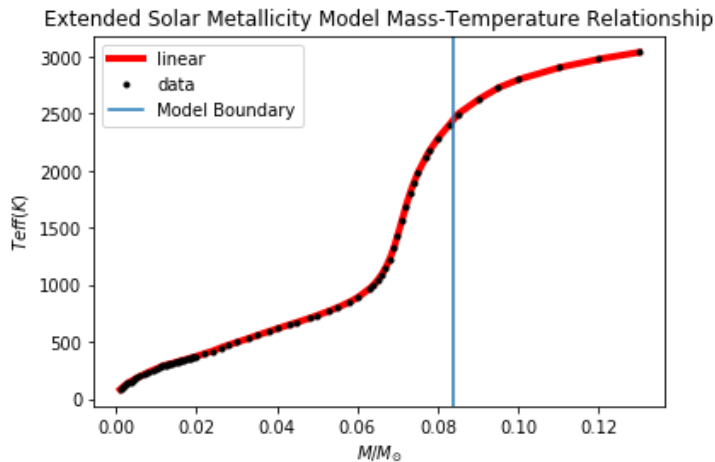


Figure 16 This figure shows the linearly interpolated mass-temperature relationship for 1000 masses between $0.01M_{\odot}$ and $0.13M_{\odot}$. The data comes from the combined solar metallicity models produced by Marley et al. (2021) and Fernandes et al. (2019). There is a large temperature change around the HBMM, but at low and high masses, the temperature slowly increases.

deuterium burning. There is another increase in luminosity in Figure 13 around $0.07M_{\odot}$ that occurs because it is around this mass that hydrogen begins fusing into helium. Figure 14 also has a similar increase in luminosity at $\sim 0.07M_{\odot}$ but it is slightly less dramatic as in Figure 13. This is because of the higher metallicity ratio which slightly adjusts the HBMM. At masses greater than the HBMM, both Figure 13 and Figure 14 gradually increase in luminosity, as is expected for main sequence stars. Generally, Figure 13 and Figure 14 are quite similar, even with the change in metallicity.

Mass and temperature are also important when investigating the transition between the stellar and substellar regimes. Similar to Figures 13 and 14, Figure 15 and Figure 16 show the mass-temperature relationships with the same two metallicities and linearly interpolated mass range. In both metallicity cases, the temperature only gradually increases until the critical HBMM is reached. At this point, when hydrogen burning begins, the temperature dramatically increases in order to sustain fusion. Figure 15 and Figure 16 clearly emphasize this large change in temperature between the stellar and substellar regions. Figure 15 and Figure 16 also show no discontinuities between the two regimes since both the Sonora and Fernandes et al. (2019) models have the same metallicity (solar metallicity).

With the model results yielding mass-luminosity and mass-temperature relationships, one can see the dramatic difference between stars and substellar objects. The differences in luminosity and temperature between stellar and substellar objects has many impacts on the underlying physical processes governing these bodies which was discussed in Chapter 1. Now with a better understanding of these models and the

transition between stars and brown dwarfs, there is one more step before an accurate comparison between the models and observational data from *GAIA* can be made.

3.3.4 Bolometric Magnitude to *GAIA* G-Band Magnitude

GAIA uses many different filters in its observations that highlight and emphasize unique features of the objects it detects. The use of such filters impacts the absolute magnitude of the objects in question. But absolute magnitude is critical to the construction of the *GAIA* luminosity functions presented in section 3.2. So to make an accurate comparison between the models and observational data, all the objects should be calculated using the same absolute magnitude. The filter used in this thesis to obtain the *GAIA* luminosity function was the G-band filter. This gives an absolute magnitude in the G-band (i.e. M_G). However, the models from Marley et al. (2021) and Fernandes et al. (2019) provide no direct information about absolute magnitude.

In order to account for this issue, a relationship between absolute bolometric magnitude, defined as a measurement of the total radiation a star emits across all wavelengths if it were placed at a distance of 10pc, and M_G was derived by cross-matching *GAIA*'s EDR3 to models of objects spanning the stellar to planetary regime produced by Filippazzo et al. (2015). Using Vizier's "X-Match" tool, *GAIA*'s observational data from EDR3 and the model data from Filippazzo et al. (2015) were matched with each other. By doing this, the bolometric magnitude could be measured using the magnitude-luminosity relationship:

$$M_{bol} = 4.74 - 2.5 \log \left(\frac{L}{L_{\odot}} \right) \quad (3.1)$$

This was possible because both EDR3 and the Filippazzo et al. (2015) model contain information about the magnitude of each object. Cross matching these two sets

of data also allows for the calculation of M_G . This was done using the distance modulus presented in Equation (2.1) where the distance was derived from the parallax.

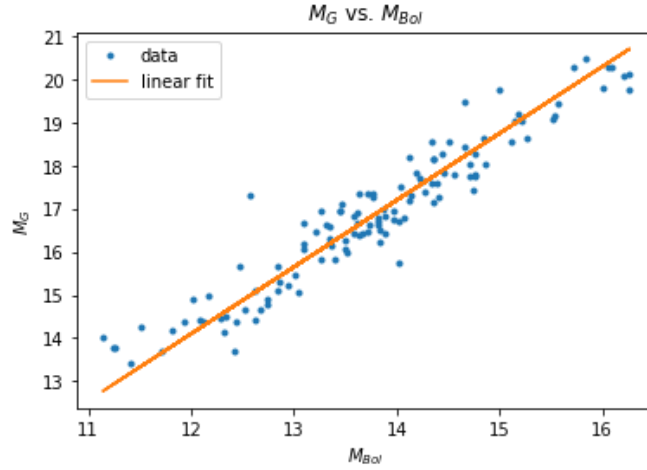


Figure 17 This figure shows the relationship between absolute bolometric magnitude and *GAIA*'s absolute magnitude in the G-band as derived from EDR3 and Filippazzo et al. (2015). Applying a linear curve fit emphasizes the seemingly linear nature of this relationship.

The purpose of doing this is to derive a relationship between M_{bol} and M_G which could then be applied to the Sonora and Fernandes et al. (2019) models to obtain values for M_G . Figure 17 shows the relationship between M_{bol} and M_G for the cross matched *GAIA* and Filippazzo et al. (2015) data. A first glance at Figure 17 suggests that there is a strong linear correlation between the two magnitudes. So, a linear curve fit was applied to derive the functional relationship between M_{bol} and M_G . Applying this curve fit yields a functional relationship between M_{bol} and M_G of:

$$M_G = 1.55 M_{bol} - 4.5 \quad (3.2)$$

Equation (3.2) now can be applied to the Sonora and Fernandes et al. (2019) models to obtain their absolute *GAIA* G-band magnitudes.

Now with the stellar/substellar models introduced in section 3.3 along with their subsequent relationships between mass, luminosity, and temperature as well as a linear relationship between M_{bol} and M_G , an accurate comparison and interpretation can be made between them and the observational luminosity functions from *GAIA* presented in section 3.2.

3.4 Interpretations of Theoretical Models and *GAIA* Luminosity Function

To fully understand what the observational luminosity functions from the *GAIA* analysis is revealing, it is useful to make a comparison to theoretical models. Section 3.3 introduced the models from Marley et al. (2021) and Fernandes et al. (2019) that were exploited in this evaluation. The Sonora models from Marley et al. (2021) were used to investigate the brown dwarf regime while the models from Fernandes et al. (2019) examined the stellar regime immediately above the HBMM. Stitching these models together provides a more complete picture into the nature of objects that are found around this critical transition.

An absolute magnitude correction needed to be accounted for so that both the models and the observational data are in the absolute *GAIA* G-band magnitude domain. By matching data from Filippazzo et al. (2015) to *GAIA*'s EDR3, a linear relationship was derived relating the absolute bolometric magnitude and the absolute *GAIA* G-band magnitude M_{bol} and M_G . This relationship is stated in Equation (3.2). Applying Equation (3.2) to the models allows them to be overplotted with the luminosity function independently obtained from *GAIA*. Figure 18 and Figure 19 show the comparison between the models and observations.

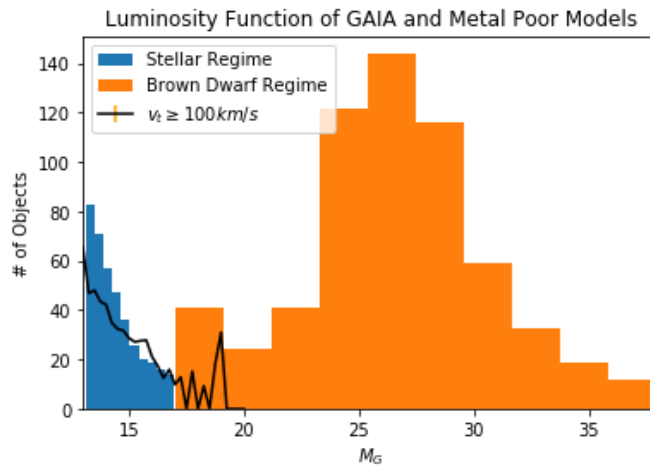


Figure 18 This figure shows a comparison between the observational luminosity function obtained from *GAIA*'s GCNS sample (black curve) and the combined models from Marley et al. (2021) (orange histogram) and Fernandes et al. (2019) (blue histogram) for 10 Gyr aged metal-poor objects. The observational luminosity function matches well with the stellar regime and penetrates into the high mass end of the brown dwarf regime.

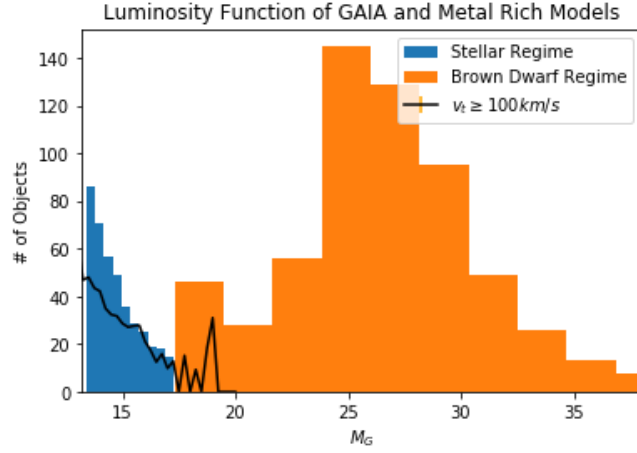


Figure 19 This diagram shows a comparison between the observational luminosity function obtained from *GAIA*'s GCNS sample (black curve) and the combined models from Marley et al. (2021) (orange histogram) and Fernandes et al. (2019) (blue histogram) for objects 10 Gyr aged objects with solar metallicity. The observational luminosity function matches with the stellar regime. The observational luminosity function also enters into the upper end of the brown dwarf regime in this case.

In both Figure 18 and Figure 19, the luminosity function for fast moving, older objects obtained from *GAIA* is denoted by the black curve. The model data in these two figures are represented by histograms describing the number of objects within an interval of M_G values. Recall from Figure 12 that the y-axis was in terms of $\left[\frac{\text{Number of Objects}}{\text{mag pc}^3}\right]$. An accurate comparison can still be made to the models by showing them in terms of $\left[\frac{\text{Number of Objects}}{\text{mag}}\right]$ and normalizing the observational luminosity function. The normalization was done by performing a reduced chi square test between the expected model distributions and the *GAIA* observational distributions and finding the minimized value.

$$\chi^2 = \sum \frac{(\text{observed} - \text{expected})^2}{\text{expected}} \quad (3.3)$$

This analysis yields a normalization constant of 925,000.

Figure 18 shows that the most old, fast-moving objects have M_G values that correspond to the cool, dim stars rather than brown dwarfs. This is known by relating the object mass to its M_G value then comparing it to the accepted HBMM. However, composition and metallicity slightly shift the HBMM. For metal-poor objects such as the ones in Figure 18, the HBMM is slightly higher than for objects with solar metallicity as shown in Figure 19. Specifically, for metal-poor objects the HBMM is $0.08M_\odot$ and for solar-metallicity objects it is $0.078M_\odot$ (Fernandes et al. 2019). Thus, most of the objects observationally detected by *GAIA* in Figure 18 and Figure 19 remain in the stellar regime. However, while most observationally detected objects are in the stellar regime, the faintest objects in both cases are found in the brown dwarf regime. Adjusting the metallicity constraint finely tunes the HBMM and will impact the number of objects found in either region. The difference in metallicities between Figure 18 and Figure 19 highlights the importance of metallicity when identifying and classifying objects in observational searches.

Even with *GAIA*'s extreme astrometric accuracy for billions of objects, a vast majority of the detected objects in the constrained GCNS dataset are late M type stars rather than brown dwarfs. The high limiting M_G magnitude of *GAIA* still barely scrapes the surface of the brown dwarf regime. However, not all hope is lost in the study of the elusive brown dwarf. *GAIA* can still study the critical HBMM transition region to a high degree of confidence shedding light on the physical mechanisms of very low mass stars and stars that will eventually transition to brown dwarfs below the HBMM as they lose mass over time. *GAIA* will also be able to explore the critical role that metallicity plays for stars and brown dwarfs very close to the HBMM.

3.5 Summary

This chapter has investigated some of the key results from the luminosity functions obtained through the analysis of *GAIA*'s GCNS dataset. For young, slow-moving objects and old, fast-moving objects, *GAIA* can calculate the luminosity function with high accuracy down to absolute magnitudes of around $M_G = +20.0$. This is quite remarkable given that *GAIA*'s limiting magnitude is +20.4 (*GAIA* Collaboration et al. 2021). As expected for both cases, the luminosity function gradually decreases as absolute magnitude increases since *GAIA* is able to detect less sources. Though this observational data is important, to better contextualize what it reveals, it was compared to recent models that investigate the brown dwarf regime and the region immediately surrounding the critical HBMM for old field objects. To make this comparison, a relationship between the absolute bolometric magnitudes found in the models and the absolute *GAIA* magnitudes in the G-band needed to be derived. Cross-matching model data with *GAIA*'s EDR3 reveal that this relationship is linear in nature. By applying this relationship, a direct comparison between the observational luminosity functions and the expected model luminosity functions was made for old metal-poor and solar metallicity objects with high tangential velocities. This was done to increase the likelihood that the objects being detected were, in fact, brown dwarfs. While it was found that the observational data aligned quite nicely with the predicted model results, most of the detected objects were very low mass stars rather than brown dwarfs. The faintest objects in the sample could potentially be brown dwarfs, but the uncertainty is substantial enough to warrant further investigations. The number of stars and brown dwarfs in the sample heavily depend on metallicity since metallicity has an impact on the HBMM. Metal-rich objects decrease the required mass for hydrogen fusion while metal-poor objects increase that critical mass.

Though it was expected that *GAIA* would be able to probe deeper into the brown dwarf regime, it will remain an excellent tool for exploring very low mass stars and high mass brown dwarfs. *GAIA* will also be a good source for investigating the physical processes of objects in the vicinity of the HBMM and the important role that metallicity plays in determining the fate of such objects.

CONCLUSIONS

In the 1960s, the first theories proposing the existence of substellar brown dwarfs were developed by Shiv Kumar. He postulated that the same process of gravitational contraction which forms stars from vast clouds of interstellar gas would also frequently produce smaller, less massive objects. These theories served to fill in the missing gap between the least massive stars on the main sequence and the most massive planets. At first, they were named “black dwarfs” or “infrared stars” before Jill Tarter of the SETI Institute coined the name “brown dwarf” in 1975.

Since then, astronomers began in earnest to search for these substellar objects. Throughout the 1980s and early 1990s, many fruitless observational searches were conducted resulting in false alarms or a failure to detect anything altogether. However, in 1995, this all changed and a new era of observational substellar astronomy was ushered in after the first *bona fide* brown dwarfs were discovered.

The years following these pivotal detections saw an explosion of new observational and theoretical work leading to the discovery of hundreds of additional brown dwarfs along with improved models describing the underlying physics that powers these objects. The field of brown dwarf astronomy has continued to rapidly develop even to this day as technological capabilities have improved, allowing for dimmer objects to be detected, even reaching down into the infrared region of the electromagnetic spectrum.

There are many tools in the arsenal that have been and are being used in the search for brown dwarfs. The earliest searches consisted of the flagship Two Micron All Sky Survey (2MASS) mission while more recent observational searches have been made using TESS, Kepler and K2, and *GAIA*. This thesis made use of publicly

available data from the *GAIA* mission. *GAIA* is a good utensil for studying brown dwarfs due to its ability to make high precision astrometric measurements for billions of sources. Specifically, *GAIA*'s EDR3 contains astrometric and photometric data for well over one billion stars and other objects. Additionally, *GAIA* has a high optical limiting magnitude ($M_G \approx +20.4$) which allows it to encompass the entire stellar regime as well as the upper end (in terms of mass) of the brown dwarf regime. While *GAIA* may not be good for understanding the lowest mass brown dwarfs, it is perfect for investigating the properties and characteristics of objects found around the critical Hydrogen Burning Minimum Mass (HBMM) of $\sim 0.08M_\odot$. One such important feature is the luminosity function.

The luminosity function is generally used to study large groups or classes of objects such as galaxies and stars in clusters. The luminosity function analysis can also be extended to brown dwarfs through a standard method which makes use of the space density. This classical technique outlined in the preceding chapters and described in detail by Schmidt (1968), Felten (1976), and Tinney (1993) was used to constrain and analyze data from *GAIA*'s Catalogue of Nearby Stars to produce local luminosity functions for stars, brown dwarfs, and other objects straddling the HBMM transition. This analysis was conducted for both young and old field objects and the resulting luminosity functions were quite similar and had low uncertainties out to high magnitudes ($M_G \approx +18.0$). As expected, at lower absolute magnitudes, the luminosity functions were greater, implying that *GAIA* is detecting more objects within a given absolute magnitude range. For higher and higher magnitudes, the corresponding luminosity functions decrease, and the uncertainties increase. This is due to *GAIA*

detecting less sources at such high magnitudes due to the optical limitations of the spacecraft's scientific instruments.

The observational luminosity functions were then compared to current brown dwarf models from Marley et al. (2021) and Fernandes et al. (2019) which emphasize objects near the HBMM transition. Making this comparison shows that *GAIA*'s observational luminosity functions agree quite well with the theoretical luminosity functions for the lowest mass stars. The observational luminosity functions also penetrate the brown dwarf regime as well. Although *GAIA* is only capable of probing the highest mass brown dwarfs (and even here, the uncertainties are quite large), it is a good tool for investigating the physical properties of objects above, below, and transitioning across the HBMM. Additional, more detailed investigations incorporating other physical properties such as metallicity and convection will need to be conducted to ensure that the objects being detected are classified correctly.

This thesis hopefully provides the groundwork for obtaining luminosity functions for low mass objects surrounding the HBMM. Moving forward, additional work can be done to better refine these luminosity functions by applying additional constraints to the data including, most notably, metallicity, temperature, and the initial mass function. The forthcoming data from the James Webb Space Telescope (*JWST*) mission will also hopefully paint a clearer picture of brown dwarfs due to its ability to study deeper into the infrared spectrum. The Large Synoptic Survey Telescope (*LSST*) slated to go online in 2023 may also provide valuable insight into brown dwarfs. *LSST*'s ability to penetrate to extremely faint magnitudes will enable it to accurately detect dim and cool objects such as brown dwarfs and exoplanets. For now, though,

GAIA has proved to be a more than capable tool for investigating the lowest mass stars, the HBMM transition region, and potentially, the elusive brown dwarf.

REFERENCES

- Allard, F. 1990, Ph.D. Thesis, Ruprecht-Karls University, Heidelberg
- Allard, F., Hauschildt, P. H., Baraffe, I., & Chabrier, G. 1996, *ApJ*, 465, L123
- Allard, F., Hauschildt, P. H., Alexander, D. R., & Starrfield, S. 1997, *ARA&A*, 35, 137
- Allard F. et al. 2001, *ApJ* 556 357
- Auddy, S., Basu, S., and Valluri, S. R., 2016, *Advances in Astronomy*, 2016
- Baraffe, I., Chabrier, G., Allard, F., & Hauschildt, P. H. 1995, *ApJ*, 446, L35
- Basri, G. et al. 1998, *ASP Conf. Ser.* 134, 394
- Bessel F.W., 1838, *Astronomische Nachrichten*, 16, 65
- Bradley J., 1727, *Philosophical Transactions of the Royal Society of London Series I*, 35, 637
- Burgasser, A. J., Kirkpatrick, J. D., Reid, I. N., Liebert, J., Gizis, J. E., & Brown, M. E. 2000a, *AJ*, 120, 473
- Burgasser, A. 2002 Ph.D. Thesis, California Institute of Technology
- Burrows, A., Hubbard, W. B., & Lunine, J. I. 1989, *ApJ*, 345, 939
- Burrows, A., Hubbard, W. B., Saumon, D., et al. (1993). *ApJ* 406, pp. 158–171.
- Burrows, A., Hubbard, W. B., Lunine, J. I., & Liebert, J. 2001, *Rev. of Modern Physics*, in press
- Burrows, A., & Liebert, J. 1993, *Rev. Mod. Phys.* 65, 301
- Burrows, A., Marley, M. S., & Sharp, C. M. 2000, *ApJ*, 531, 438
- Burrows, A., & Sharp, C. M. 1999, *ApJ*, 512, 843
- Burrows, A., et al. 1997, *ApJ*, 491, 856
- Chabrier, G., & Baraffe, I. 2000, *ARA&A*, 38, 337
- Chabrier, G., Baraffe, I., Allard, F., & Hauschildt, P. 2000a, *ApJ*, 542, 464

- Chabrier, G., Baraffe, I., & Plez, B. 1996, *ApJ*, 459, L91
- Chabrier, G., Baraffe, I., 1997. *Astr. Astrophys.*, 327, 1039.
- Chandrasekhar, S. 1939, *An Introduction to the Study of Stellar Structure* (New York: Dover)
- Crovisier, J. 1978, *Astr. Ap.*, 70, 43.
- D'Antona, F., & Mazzitelli, I. 1985, *ApJ*, 296, 502
- Dickey, J. M., Salpeter, E. E., and Terzian, Y. 1978, *ApJ. Suppl*, 36, 77.
- ESA (ed.), 1997, *The HIPPARCOS and TYCHO catalogues. Astrometric and photometric star catalogues derived from the ESA HIPPARCOS Space Astrometry Mission*, vol. 1200 of ESA Special Publication
- Fegley, B., & Lodders, K. 1996, *ApJ*, 472, L37
- Felten, J. E. 1976, *ApJ*, 207, 700
- Fernandes, C. S., et al. 2019, *ApJ*, 879, 94
- Filippazzo, J., et al. 2015, 205, *ApJ*, 810, 158
- Gaia Collaboration, Brown, Anthony G.A., Vallenari, A., Prusti, T., de Bruijne, J. H.J., et al., 2020, *Gaia early data release 3. summary of the contents and survey properties*, *Astron. Astrophys.*
- Gaia Collaboration, Prusti, T., de Bruijne, J. H. J., et al. 2016, *A&A*, 595, A1
- Gaia Collaboration, R. L. Smart, L. M. Sarro, J. Rybizki, C. Reylé, A. C. Robin, N. C. Hambly, U. Abbas, M. A. Barstow, J. H. J. de Bruijne, et al., 2021, *A&A*, 649 A6
- Grossman, A. S. and Graboske, H. C., 1973, *ApJ*, 180, 195–198
- Halley E., 1717, *Philosophical Transactions of the Royal Society of London Series I*, 30, 736
- Henderson T., 1840, *MmRAS*, 11, 61
- Hansen, C. J., & Kawaler, S. D. 1994, *Stellar Interiors: Physical Principles, Structure, and Evolution* (New York: Springer-Verlag)

- Hauschildt, P. H., Lowenthal, D. K., & Baron, E. 2001, *ApJS*, 134, 323
- Hayashi, C. 1961, *PASJ*, 13, 450
- Hayashi, C. and Nakano, T. (1963). *Progress of Theoretical Physics*, 30, 460-474.
- Hoxie, D. T. 1970, *ApJ*, 161, 1083
- Kirkpatrick, J. D., et al. 1999b, *ApJ*, 519, 802
- Kumar, S.S., 1963. *ApJ*, 137, 1121-1125.
- Lecavelier, A., & Lissauer, J.J. 2022, *New Astronomy Reviews*, 94
- Lindgren L., Bastian U., 2011, In: *EAS Publications Series*, vol. 45 of *EAS Publications Series*, 109–114
- Lodders, K. 1999, *ApJ*, 519, 793
- Lunine, J. I., Hubbard, W. B., Burrows, A., Wang, Y.P., & Garlow, K. 1989, *ApJ*, 338, 314
- Lunine, J. I., Hubbard, W. B., & Marley, M. S. 1986, *ApJ*, 310, 238
- Marley, M. S., Saumon, D., Guillot, T., Freedman, R. S., Hubbard, W. B., Burrows, A., & Lunine, J. I. 1996, *Science*, 272, 1919
- Marley, M., et al. 2021, *ApJ*, 920, 85
- Mould, J. R. 1975, *A&A*, 38, 283
- . 1976, *A&A*, 48, 443
- Oppenheimer, B. R., Kulkarni, S. R., Matthews, K., & Nakajima, T. 1995, *Science*, 270, 1478
- Piskunov, N., Wood, B. E., Linsky, J. L., Dempsey, R. C., & Ayres, T. R. 1997, *ApJ*, 474, 315
- Saumon, D., Bergeron, P., Lunine, J. I., Hubbard, W. B., & Burrows, A. 1994, *ApJ*, 424, 333
- Rebolo, R., Martín, E. L., & Magazzu, A. 1992, *ApJ*, 389, L83
- Rebolo, R., Zapatero Osorio, M. R., & Martín, E. L. 1995, *Nature*, 377, 129

- Saumon, D., Chabrier, G., & Van Horn, H. M. 1995, *ApJS*, 99, 713
- Schmidt, M. 1968, *ApJ*, 151, 393
- Shu, F. H. and Adams, F. C., “Star formation and the circumstellar matter of young stellar objects.”, *Circumstellar Matter*, 1987, vol. 122, p. 7.
- Shu, F. H., Adams, F. C., & Lizano, S. 1987, *ARA&A*, 25, 23
- Stahler, S. W. 1988, *PASP*, 100, 1474
- Stevenson, D. J. 1978, *Proc. Astr. Soc. Australia*, 3, 227.
- Stevenson, D. J. 1991, *ARA&A*, 29, 163
- Tarter, J. 1975, Ph.D. Thesis, University of California, Berkeley
- Tholen, D. J., Tejfel, V. G., & Cox, A. N. 2000, in *Allen’s Astrophysical Quantities*, Fourth Edition, ed. A. N. Cox (New York: Springer-Verlag), p. 293
- Tinney, C. G., Reid, I. N., & Mould, J. R. 1993, *ApJ*, 414, 254
- Tsuji, T., Ohnaka, K., Aoki, W., & Nakajima, T. 1996, *A&A*, 308, L29
- Vandenberg, D. A., Hartwick, F. D. A., & Dawson, P. 1983, *ApJ*, 266, 747
- von Struve O.W., 1840, *Astronomische Nachrichten*, 17, 177